

¹
² Susceptible host dynamics explain pathogen resilience to
³ perturbations

⁴

⁵ Sang Woo Park, . . . , Bryan T. Grenfell, Sarah Cobey

⁶ Abstract

⁷ A major priority for epidemiological research in the time of anthropogenic change
⁸ is understanding how infectious disease dynamics respond to perturbations. Inter-
⁹ ventions to slow the spread of SARS-CoV-2 significantly disrupted the transmission
¹⁰ of other human pathogens. As interventions lifted, whether and when respiratory
¹¹ pathogens would eventually return to their pre-pandemic dynamics remains to be
¹² answered. Here, we present a framework for estimating pathogen resilience based on
¹³ how fast epidemic patterns return to their pre-pandemic, endemic dynamics and an-
¹⁴ alyze time series data from Hong Kong, Canada, Korea, and the US. By quantifying
¹⁵ the resilience of common respiratory pathogens, we are able to predict when each
¹⁶ pathogen will eventually return to its pre-pandemic, endemic dynamics. Our pre-
¹⁷ dictions closely match the observed deviations (or lack thereof) from its pre-COVID
¹⁸ dynamics. Discrepancies between predicted and observed dynamics indicate the
¹⁹ long-term impact of pandemic perturbations, suggesting that some pathogens may
²⁰ be converging to a different endemic cycle. Finally, we show that the replenishment
²¹ rate of the susceptible pool is a key determinant of pathogen resilience, which in
²² turn determines the sensitivity of a system to stochastic perturbations. Overall, our
²³ analysis highlights the persistent nature of common respiratory pathogens compared
²⁴ to vaccine-preventable infections, such as measles.

25 Non-pharmaceutical interventions to slow the spread of SARS-CoV-2 disrupted
 26 the transmission of other human respiratory pathogens, adding uncertainties to their
 27 future epidemic dynamics and their public health burden [1]. As interventions lifted,
 28 large heterogeneities in outbreak dynamics were observed across different pathogens
 29 in different countries, with some pathogens exhibiting earlier and faster resurgences
 30 than others [2, 3, 4]. Heterogeneities in the overall reduction in transmission and the
 31 timing of re-emergence likely reflect differences in intervention patterns, pathogen
 32 characteristics, immigration/importation from other countries, and pre-pandemic
 33 pathogen dynamics [5]. Therefore, comparing the differential impact of the pan-
 34 *demic* perturbations across pathogens can provide unique opportunities to learn
 35 about underlying pathogen characteristics, such as their transmissibility or duration
 36 of immunity, from heterogeneities in re-emergence patterns [6].

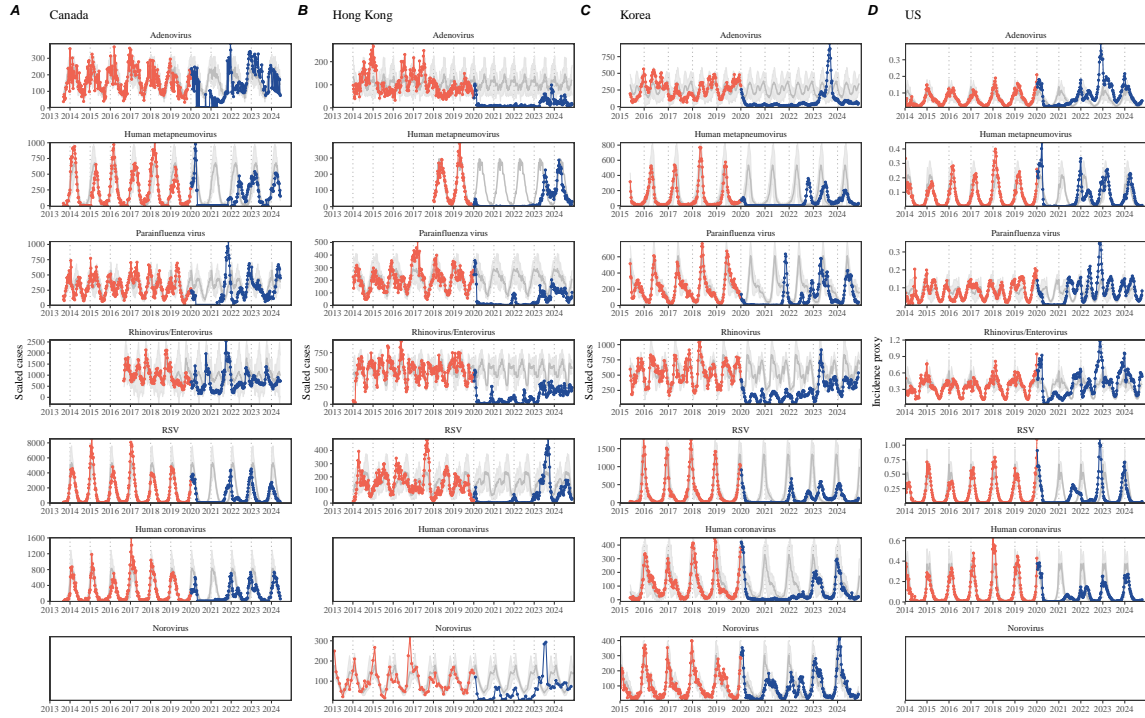


Figure 1: Observed heterogeneity in responses to pandemic perturbations across respiratory pathogens and norovirus in (A) Canada, (B) Hong Kong, (C) Korea, and (D) US. Red points and lines represent data before 2020. Blue points and lines represent data since 2020. Gray lines and shaded regions represent the mean seasonal patterns and corresponding 95% confidence intervals around the mean. Mean seasonal patterns were calculated by aggregating cases before 2020 into 52 weekly bins and taking the average in each week. Cases were scaled to account for changes in testing patterns (Materials and Methods).

37 Even though more than five years have passed since the emergence of SARS-CoV-
 38 2, we still observe persistent changes in pathogen dynamics following the pandemic

39 perturbations. For example, compared to pre-pandemic, seasonal patterns, human
40 metapneumovirus in Korea seem to circulate at lower levels, whereas RSV in Ko-
41 rea seems to exhibit different seasonality (Figure 1). These observations suggest a
42 possibility for a fundamental change in pathogen dynamics following the pandemic
43 perturbations, which can be driven by a permanent shift in either human behavior
44 or population-level immunity [7, 8]. The possibility of a long-lasting impact of the
45 pandemic perturbations poses an important question for future infectious disease
46 dynamics: can we predict whether and when other respiratory pathogens will even-
47 tually return to their pre-pandemic dynamics? *[SWP: You suggested: I would say
48 something about the dynamics of these pathogens not being well understood, but
49 I've since rewritten the most of intro and I'm not sure where I would fit this. If you
50 have any suggestions, let me know...]*

51 So far, the majority of epidemiological analyses of respiratory pathogens in the
52 context of the pandemic perturbations have focused on characterizing the timing of
53 rebound [1, 9, 5]. Instead, we seek to characterize how fast a pathogen returns to its
54 pre-pandemic dynamics. These two concepts have subtle but important differences:
55 for example, it took more than 3 years for human metapneumovirus to rebound in
56 Hong Kong but the observed epidemic patterns in 2024 are similar to pre-pandemic
57 seasonal means, suggesting a rapid return to pre-pandemic dynamics following a
58 perturbation (Figure 1). Measuring this rate of return is particularly useful because
59 it allows us to quantify the ecological resilience of a host-pathogen system [10, 11,
60 12, 13].

61 In this study, we lay out theoretical and statistical approaches to characterizing
62 the resilience of a host-pathogen system based on how fast the system recovers from
63 perturbation. We begin by laying out a few representative scenarios that capture
64 the potential impact of pandemic perturbations on endemic pathogen dynamics and
65 illustrate how resilience can be measured by comparing the pre- and post-pandemic
66 dynamics of susceptible and infected hosts. In practice, information on susceptible
67 hosts is often unavailable, making this theoretical approach infeasible. Instead, we
68 utilize a mathematical technique to reconstruct empirical attractors from the data
69 [14], which allows us to measure the rate at which the host-pathogen system ap-
70 proaches this empirical attractor after a perturbation; this rate corresponds to the
71 resilience of the host-pathogen system. We use this method to analyze pathogen
72 surveillance data for respiratory and non-respiratory pathogens from Canada, Hong
73 Kong, Korea, and the US. Finally, we show that susceptible host dynamics explain
74 variation in pathogen resilience and further link pathogen resilience to responses to
75 perturbations caused by demographic stochasticity, thereby providing a direct link
76 between pathogen resilience and persistence.

⁷⁷ Conceptual introduction to pathogen resilience

⁷⁸ In classical ecological literature, the resilience of an ecological system is measured by
⁷⁹ the rate at which the system returns to its reference state following a perturbation
⁸⁰ [10, 11, 12, 13]. This rate corresponds to the largest real part of the eigenvalues of
⁸¹ the linearized system near equilibrium—here, we refer to this value as the *intrinsic*
⁸² resilience of the system, which represents the expected rate of return from perturbed
⁸³ states. In practice, we rarely know the true model describing population-level dy-
⁸⁴ namics of common respiratory pathogens, limiting our ability to infer the intrinsic
⁸⁵ resilience of a system. Instead, we can still measure the *empirical* resilience of a
⁸⁶ host-pathogen system by looking at how fast the system returns to the pre-pandemic,
⁸⁷ endemic dynamics after pandemic perturbations are lifted.

⁸⁸ As an example, we begin with a simple Susceptible-Infected-Recovered-Susceptible
⁸⁹ (SIRS) model with seasonally forced transmission and demography (i.e., birth and
⁹⁰ death). The SIRS model is the simplest model that allows for the waning of im-
⁹¹ munity and is commonly used for modeling the dynamics of respiratory pathogens
⁹² [15]. First, consider a pandemic perturbation that reduces transmission by 50% for 6
⁹³ months starting in 2020, which causes epidemic patterns to deviate from their origi-
⁹⁴ nal stable annual cycle for a short period of time and eventually come back (Figure
⁹⁵ 2A). To measure the resilience of this system empirically, we first need to be able to
⁹⁶ measure the distance from its pre-pandemic attractor. There are many ways we can
⁹⁷ measure the distance from the attractor, but for illustrative purposes, we choose one
⁹⁸ of the most parsimonious approaches: that is, we look at how the susceptible (S) and
⁹⁹ infected (I) populations change over time and measure the distance on the SI phase
¹⁰⁰ plane (Figure 2B). In this simple case, the locally estimated scatterplot smoothing
¹⁰¹ (LOESS) fit indicates that the distance from the attractor decreases exponentially
¹⁰² (linearly on a log scale) on average (Figure 2C). Furthermore, the overall rate of re-
¹⁰³ turn approximates the intrinsic resilience of the seasonally unforced system (Figure
¹⁰⁴ 2C).

¹⁰⁵ Alternatively, pandemic perturbations can have a lasting impact on the pathogen
¹⁰⁶ dynamics; as an example, we consider a scenario in which a 10% reduction in trans-
¹⁰⁷ mission persists even after the major pandemic perturbations are lifted (Figure 2D–
¹⁰⁸ F). In such cases in practice, we cannot know whether the pathogen will return to
¹⁰⁹ its original cycle or a different cycle until many years have passed, and we cannot
¹¹⁰ measure the distance to the new unknown attractor that the system might eventu-
¹¹¹ ally approach. Nonetheless, we can still measure the distance from the pre-pandemic
¹¹² attractor and ask how the distance changes over time (Figure 2E). The LOESS fit
¹¹³ suggests that the distance from the pre-pandemic attractor will initially decrease ex-
¹¹⁴ponentially on average (equivalently, linearly on a log scale) and eventually plateau
¹¹⁵ (Figure 2F). Here, a permanent 10% reduction in transmission rate slows the system,
¹¹⁶ which causes the distance from the pre-pandemic attractor initially to decrease at a
¹¹⁷ slower rate (Figure 2F) than it would have otherwise (Figure 2C) before plateauing
¹¹⁸ at a fixed distance between the two attractors. This example shows that resilience

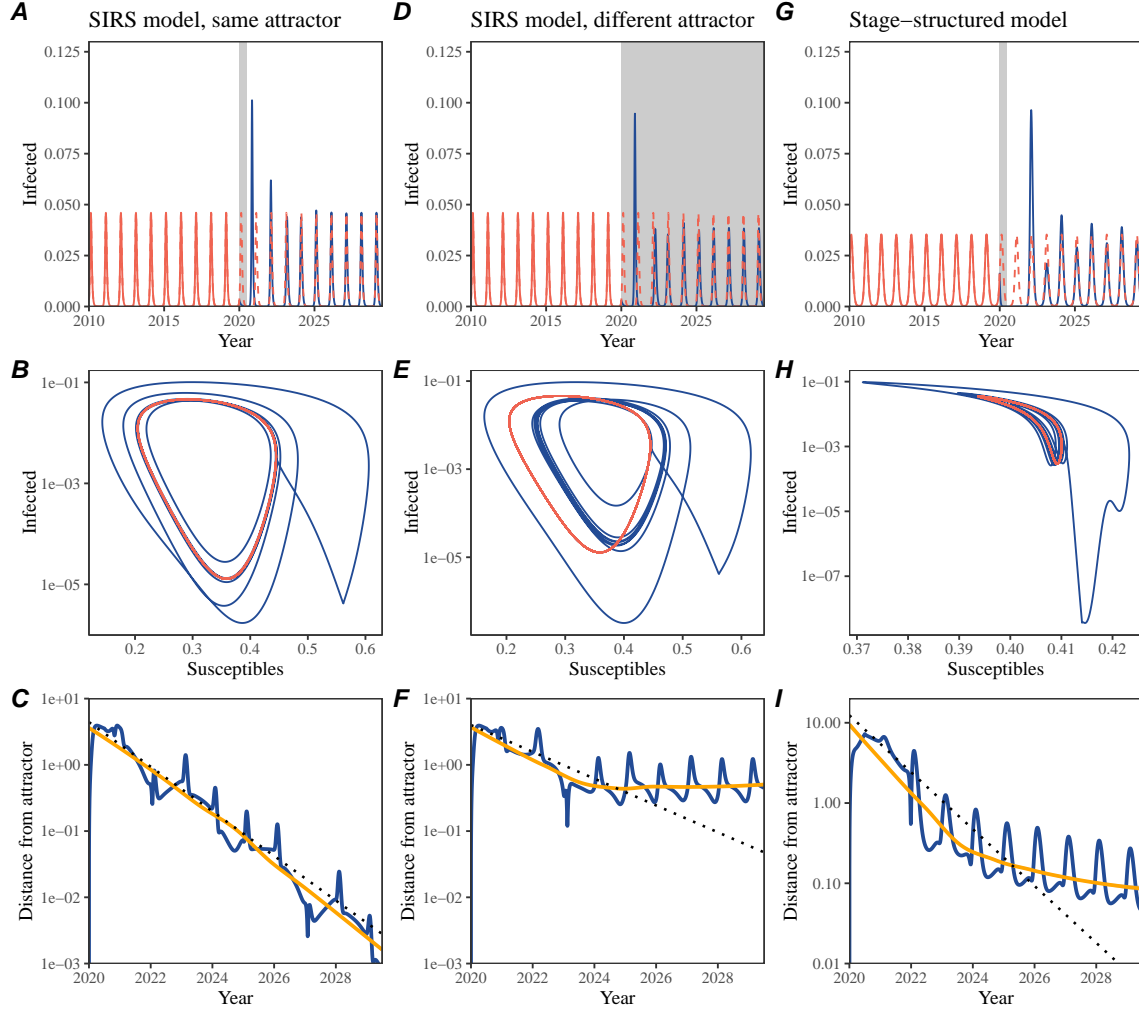


Figure 2: A simple method to measure pathogen resilience following pandemic perturbations across different scenarios. (A, D, G) Simulated epidemic trajectories across various models. Red and blue solid lines represent epidemic dynamics before and after pandemic perturbations are introduced, respectively. Red dashed lines represent counterfactual epidemic dynamics in the absence of perturbations. Gray regions indicate the duration of perturbations. (B, E, H) Phase plane representation of the time series in panels A, D, and G alongside the corresponding susceptible host dynamics. Red and blue solid lines represent epidemic trajectories on an SI phase plane before and after perturbations are introduced, respectively. (C, F, I) Changes in logged distance from the attractor over time. Blue lines represent the logged distance from the attractor. Orange lines represent the locally estimated scatterplot smoothing (LOESS) fits to the logged distance from the attractor. Dotted lines show the intrinsic resilience of the seasonally unforced system.

is not necessarily an intrinsic property of a specific pathogen. Instead, pathogen re-

120 resilience is a property of a specific attractor that a host-pathogen system approaches,
121 which depends on both pathogen and host characteristics.

122 Finally, transient phenomena can further complicate the picture (Figure 2G–I).
123 For example, a stage-structured model initially exhibits a stable annual cycle, but
124 perturbations from a 10% reduction in transmission for 6 months cause the epidemic
125 to shift to biennial cycles (Figure 2G). The system eventually approaches the original
126 pre-pandemic attractor (Figure 2H), suggesting that this biennial cycle is a transient
127 phenomenon. The LOESS fit indicates that the distance from the attractor initially
128 decreases exponentially at a rate that is consistent with the intrinsic resilience of
129 the seasonally unforced stage-structured system, but the rate of decrease decelerates
130 with the damped oscillations (Figure 2I). This behavior is also referred to as a ghost
131 attractor, which causes long transient dynamics and slow transitions [16]. Strong
132 seasonal forcing in transmission can also lead to transient phenomena for a simple
133 SIRS model, causing a slow return to pre-perturbation dynamics (Supplementary
134 Figure S1).

135 This empirical approach allows us to measure the resilience of a two-strain host-
136 pathogen system even when we have incomplete observation of the infection dynam-
137 ics. Simulations from a simple two-strain system illustrate that separate analyses of
138 individual strain dynamics (e.g., RSV A vs B) and a joint analysis of total infections
139 (e.g., total RSV infections) yield identical resilience estimates (Supplementary Fig-
140 ure S2, 3). This is expected because the dynamics of two strains (or two pathogens)
141 around the attractor in a coupled system are described by the same set of eigen-
142 values and eigenvectors, meaning that both strains should exhibit identical rates of
143 returns following a perturbation. Analogous to a single system, strong seasonal forc-
144 ing in transmission can cause the system to slow down through transient phenomena
145 (Supplementary Figure S4).

146 These observations indicate three possibilities. First, we can directly estimate the
147 empirical resilience of a host-pathogen system by measuring the rate at which the
148 system approaches an attractor, provided that we have a way to quantify the distance
149 from the attractor. The empirical approach to estimating pathogen resilience is
150 particularly convenient because it does not require us to know the true underlying
151 model; estimating the intrinsic resilience from fitting misspecified models can lead
152 to biased estimates (Supplementary Figure S5). Second, resilience estimates allow
153 us to make phenomenological predictions about the dynamics of a host-pathogen
154 system following a perturbation. Assuming that the distance from the attractor will
155 decrease exponentially over time, we can obtain a ballpark estimate for when the
156 system will reach an attractor; this prediction necessarily assumes that there won't
157 be permanent changes in pathogen dynamics (Figure 2F) or a long-term transient
158 phenomenon (Figure 2I). Finally, a change in the rate of an exponential decrease in
159 the distance from the attractor can provide information about whether the system
160 has reached an alternative attractor, or a ghost attractor, that is different from the
161 original, pre-pandemic attractor. These alternative attractors may reflect continued
162 perturbations from permanent changes in transmission patterns as well as changes in

163 immune landscapes. There will be periods of time when it is difficult to tell whether
164 pathogen dynamics are still diverging from its original attractor or have begun to
165 converge to an attractor; now that several years have passed since interventions have
166 been lifted, we expect many respiratory pathogens to have had sufficient time to
167 begin returning to their post-intervention attractors.

168 Inferring pathogen resilience from real data

169 Based on these observations, we now lay out our approach to estimating pathogen
170 resilience from real data (Figure 3). We then test this approach against simulations
171 and apply it to real data.

172 So far, we focused on simple examples that assume a constant transmission re-
173 duction. However, in practice, the impact of pandemic perturbations on pathogen
174 transmission is likely more complex (Figure 3A), reflecting introduction and relax-
175 ation of various intervention strategies. In some cases, strong perturbations can even
176 lead to a local fadeout, requiring immigration from another location for epidemic re-
177 emergence. These complexities can lead to longer delays between the introduction of
178 pandemic perturbations and pathogen re-emergence as well as temporal variation in
179 outbreak sizes (Figure 3B): in this example, continued transmission reduction from
180 interventions limits the size of the first outbreak in 2021 following the emergence,
181 allowing for a larger outbreak in 2022 when interventions are further relaxed.

182 Previously, we relied on the dynamics of susceptible and infected hosts to com-
183 pute the distance from the attractor (Figure 2), but information on susceptible hosts
184 is rarely available in practice. In addition, uncertainties in case counts due to obser-
185 vation error as well as multiannual cycles in the observed epidemic dynamics (e.g.,
186 adenovirus circulation patterns in Hong Kong and Korea) add challenges to defin-
187 ing pre-pandemic attractors, which limits our ability to measure the distance from
188 the attractor. To address these challenges, we can reconstruct an empirical attrac-
189 tor by utilizing Takens' theorem [14], which states that an attractor of a nonlinear
190 multidimensional system can be mapped onto a delayed embedding (Materials and
191 Methods). For example, we can use delayed logged values of pre-pandemic cases $C(t)$
192 (Figure 3C) to reconstruct the attractor:

$$\langle \log(C(t) + 1), \log(C(t - \tau) + 1), \dots, \log(C(t - (M - 1)\tau) + 1) \rangle, \quad (1)$$

193 where the delay τ and embedding dimension M are determined based on autocor-
194 relations and false nearest neighbors, respectively [17, 18]. We can then apply the
195 same delay and embedding dimensions to the entire time series to determine the
196 position on a multi-dimensional state space (Figure 3D), which allows us to mea-
197 sure the nearest neighbor distance between the current state of the system and the
198 empirical pre-pandemic attractor (Figure 3E). In theory, we can now quantify how
199 fast this distance decreases by fitting a linear regression on a log scale, where the
200 slope of the linear regression corresponds to pathogen resilience. However, resulting

estimates of pathogen resilience can be sensitive to choices about embedding delays and dimensions; for example, using longer delays and higher dimensions tends to smooth out temporal variations in the distance from the attractor (Supplementary Figure S6).

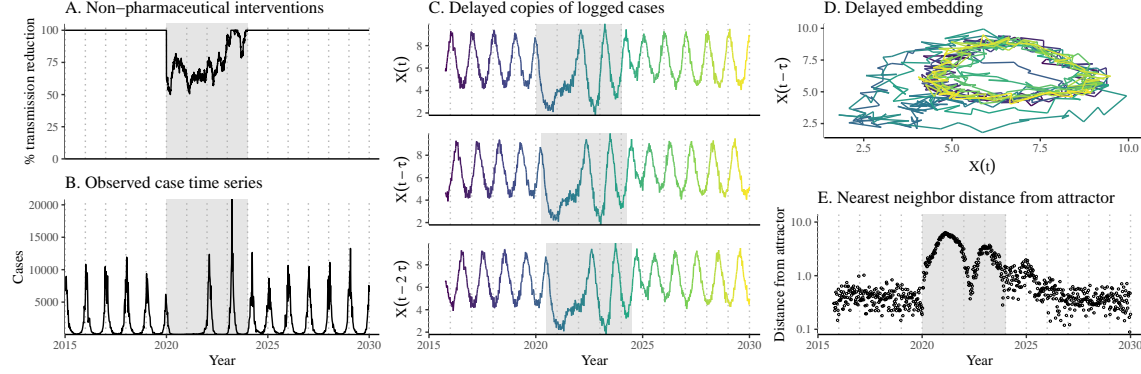


Figure 3: A schematic diagram explaining the inference of pathogen resilience from synthetic data. (A) A realistic example of simulated pandemic perturbations, represented by a relative reduction in transmission. (B) The impact of the synthetic pandemic perturbation on epidemic dynamics simulated using a SIRS model with demographic stochasticity. (C) Generating delayed copies of the logged time series allows us to obtain an embedding. (D) Two dimensional representation of an embedding. (E) Delayed embedding allows us to calculate the nearest neighbor distance from the empirical attractor, which is determined based on the pre-pandemic time series. This distance time series can be used to infer pathogen resilience after choosing an appropriate window for linear regression.

Complex changes in the distance from the attractor suggest that estimating pathogen resilience from linear regression will be particularly sensitive to our choice of fitting windows for the regression (Figure 3E). Therefore, before we tried estimating resilience from real data, we explored an automated window selection criterion for linear regression and test it against randomized, stochastic simulations across a wide range of realistic pandemic perturbation shapes; in doing so, we also explored optimal choices for embedding dimensions and evaluated our choices for fitting window parameters and embedding dimensions by quantifying correlation coefficients between the estimated resilience and the intrinsic resilience of a seasonally unforced system (Materials and Methods). Overall, we find large variation in estimation performances with correlation coefficient ranging from 0.21 to 0.61 (Supplementary Figure S7). In almost all cases, the automated window selection approach outperformed a naive approach that uses the entire time series, starting from the peak distance (Supplementary Figure S7).

Based on the best performing window selection criteria and embedding dimension, we applied this approach to pathogen surveillance data presented in Figure 1 (Materials and Methods). For each time series, we applied Takens' theorem in-

222 dependently to reconstruct the empirical attractor and obtained the corresponding
223 time series of distances from attractors (Supplementary Figure S8). Then, we use
224 the automated window selection criterion to fit a linear regression and estimate the
225 empirical resilience for each pathogen in each country (Supplementary Figure S8);
226 the window selection criterion gave poor regression window for three cases (norovirus
227 in Hong Kong and Korea and Rhinovirus/Enterovirus in the US), leading to unreal-
228 istically low resilience estimates, and so we used ad-hoc regression windows instead
229 (Supplementary Figure S9; Materials and Methods).

230 For all pathogens we consider, resilience estimates fall between 0.4/year and
231 1.8/year (Figure 4A). We estimate the mean resilience of common respiratory pathogens
232 to be 0.99/year (95% CI: 0.81/year–1.18/year). As a reference, this is \approx 7.5 times
233 higher than the intrinsic resilience of pre-vaccination measles in England and Wales
234 (\approx 0.13/year). Finally, resilience estimates for norovirus are comparable to those of
235 common respiratory pathogens: 1.44/year (95%CI: 1.01/year–1.87/year) for Hong
236 Kong and 1.07/year (95%CI: 0.86/year–1.29/year) for Korea. Based on a simple
237 ANOVA test, we do not find significant differences in resilience estimates across
238 countries ($p = 0.25$) or pathogens ($p = 0.67$).

239 [SWP: You suggested “I think we probably need to spell out a bit more that
240 long-term changes in the transmission rate (or some other parameter) mean the at-
241 tractor is permanently different and the distance should remain nonzero” and I think
242 we’ve done that enough early on with current revisions so I don’t feel like we need
243 to do it again here. Let me know what you think.] Using resilience estimates, we
244 predicted when each pathogen would hypothetically return to their pre-pandemic
245 dynamics, assuming no long-term change in the attractor. Specifically, we extend
246 our linear regression fits to distance-from-attractor time series and ask when the pre-
247 dicted regression line will cross a threshold value; since we relied on nearest neighbor
248 distances, pre-pandemic distances are always greater than zero (Figure 3E), meaning
249 that we can use the mean of pre-pandemic distances as our threshold.

250 We predict that a return to pre-pandemic cycles would be imminent for most
251 pathogens (Figure 4B). In particular, we predict that 12 out of 23 pathogens should
252 have already returned before the end of 2024. For almost all pathogens that are
253 predicted to have returned already, the observed epidemic dynamics show clear con-
254 vergence towards their pre-pandemic seasonal averages, confirming our predictions
255 (Figure 4C). However, there are a few exceptions, including norovirus in Hong Kong
256 and Rhinovirus/Enterovirus in the US, where the observed epidemic dynamics in
257 2024 exhibit clear deviation from their pre-pandemic seasonal averages (Figure 4C).
258 These observations suggest a possibility that some common respiratory pathogens
259 may have converged to different attractors or are still exhibiting non-equilibrium
260 dynamics. In contrast, pathogens that are predicted to have not returned yet also
261 show clear differences from their pre-pandemic seasonal averages; as many of these
262 pathogens are predicted to return in 2025–2026, we may be able to test these pre-
263 dictions in near future (Supplementary Figure S10). Our reconstructions of distance
264 time series and estimates of pathogen resilience and expected return time are gener-

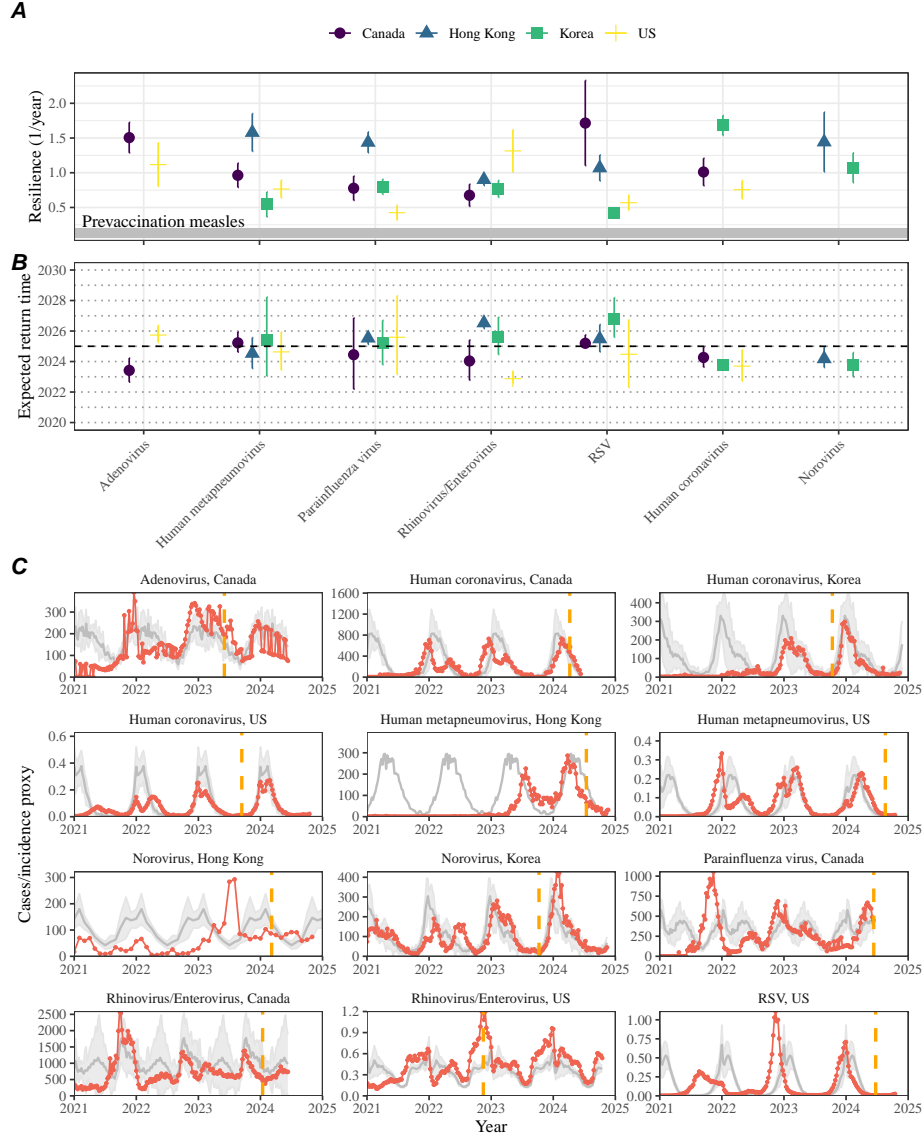


Figure 4: Summary of resilience estimates and predictions for return time. (A) Estimated pathogen resilience. The gray horizontal line represents the intrinsic resilience of pre-vaccination measles dynamics. (B) Predicted timing of when each pathogen will return to their pre-pandemic cycles. The dashed line in panel B indicates the end of 2024 (current observation time). Error bars represent 95% confidence intervals. (C) Observed dynamics for pathogen that are predicted to have returned before the end of 2024. Red points and lines represent data before 2020. Gray lines and shaded regions represent the mean seasonal patterns and corresponding 95% confidence intervals around the mean, previously shown in Figure 1. Orange vertical lines represent the predicted timing of return.

265 ally robust to choices of embedding dimensions (Supplementary Figure S11–12).

266 **Susceptible host dynamics explain variation in pathogen
267 resilience**

268 So far, we focused on quantifying pathogen resilience from the observed patterns
269 of pathogen re-emergence following pandemic perturbations. But what factors de-
270 termine how resilient a host-pathogen system is? Here, we use the SIRS model to
271 show that susceptible host dynamics are the key determinants of pathogen resilience.
272 To do so, we vary the basic reproduction number \mathcal{R}_0 , which represents the average
273 number of secondary infections caused by a newly infected individual in a fully sus-
274 ceptible population, and the duration of immunity and compute intrinsic resilience
275 for each parameter.

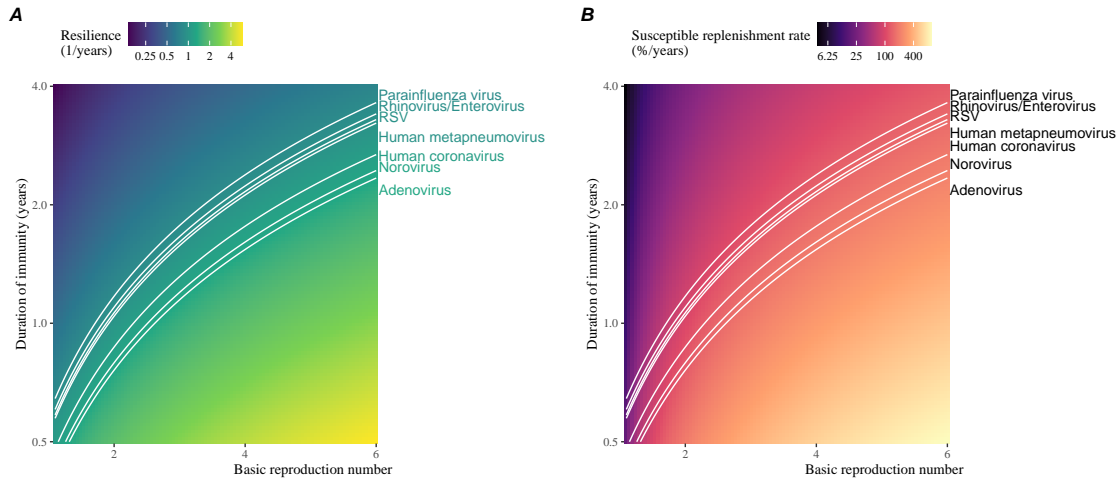


Figure 5: **Linking pathogen resilience to epidemiological parameters and susceptible host dynamics.** (A) The heat map represents intrinsic resilience as a function of the basic reproduction number \mathcal{R}_0 and the duration of immunity. (B) The heat map represents per-capita susceptible replenishment rate as a function of the basic reproduction number \mathcal{R}_0 and the duration of immunity. The standard SIRS model is used to compute intrinsic resilience and per-capita susceptible replenishment rate. Lines correspond to a set of parameters that are consistent with mean resilience estimates for each pathogen. Pathogens are ranked based on their mean resilience estimates, averaged across different countries.

276 We find an increase in \mathcal{R}_0 and a decrease in duration of immunity correspond
277 to an increase in pathogen resilience (Figure 5A). These variations can be under-
278 stood in terms of the susceptible host dynamics, where faster per-capita susceptible
279 replenishment rate causes the system to be more resilient (Figure 5B). This rate can

280 be expressed as a ratio between absolute rate at which new susceptibles enter the
281 population and the equilibrium number of susceptible individuals in the population,
282 \bar{S} . Therefore, both higher \mathcal{R}_0 and shorter duration of immunity can drive faster
283 per-capita susceptible replenishment rate (Figure 5B), especially because higher \mathcal{R}_0
284 leads to lower \bar{S} .

285 We can also rank different pathogens based on the average values of empirical
286 resilience computed previously, which allows us to determine a set of parameters that
287 are consistent with the estimated resilience (Figure 5A). Across all pathogens we
288 consider, except for bocavirus and norovirus, we estimate that the average duration
289 of immunity is likely to be short (< 4 years) across a plausible range of \mathcal{R}_0 (< 6).
290 These rankings further allow us to map each pathogen onto a set of SIRS parameters
291 that are consistent with its empirical resilience (Figure 5A) and obtain a plausible
292 range of susceptible replenishment rates for each pathogen (Figure 5B). However, we
293 note that there is no one-to-one correspondence between susceptible replenishment
294 rates and pathogen resilience, leading to a wide uncertainty in the estimates for
295 susceptible replenishment rates (Figure 5B).

296 **Pathogen resilience determines sensitivity to stochastic perturbations**

297

298 Beyond the pandemic perturbations, we expect host-pathogen systems to experience
299 continued perturbations of varying degrees from changes in epidemiological conditions,
300 such as human behavior, climate, and viral evolution. These perturbations
301 can also arise from demographic stochasticity, which is inherent to any ecological
302 systems. Here, we use a seasonally unforced SIRS model with birth/death to explore
303 how resilience of a host-pathogen system determines the sensitivity to perturbations
304 caused by demographic stochasticity (Materials and Methods).

305 We find that resilience of a host-pathogen system determines the amount of deviation
306 from the deterministic trajectory caused by demographic stochasticity, with less
307 resilient systems experiencing larger deviations (Figure 6). Notably, less resilience
308 systems also exhibit slower epidemic cycles; the periodicity of this epidemic cycle
309 matches those predicted by the intrinsic periodicity of the system (Supplementary
310 Figure S13). These conclusions are robust for the seasonally forced SIRS model
311 (Supplementary Figure S14),

312 **Discussion**

313 The pandemic interventions have caused major disruptions to circulation patterns of
314 both respiratory and non-respiratory pathogens, adding challenges to predicting their
315 future dynamics [1, 2, 3, 4]. However, these perturbations offer large-scale natural
316 experiments for understanding how different pathogens respond to perturbations. In

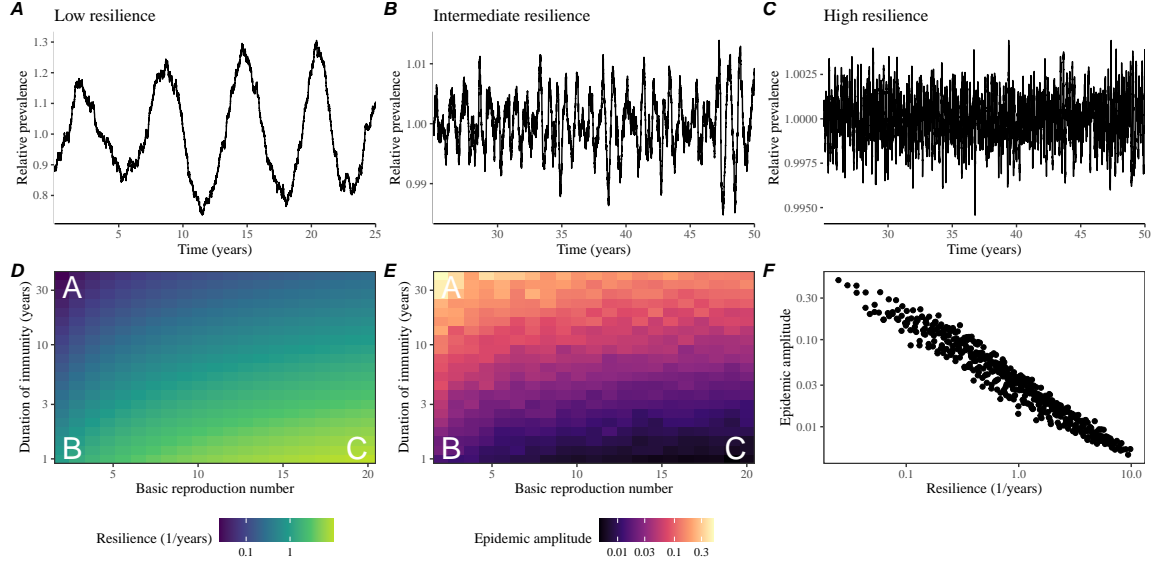


Figure 6: Linking resilience of a host-pathogen system to its sensitivity to stochastic perturbations. (A–C) Epidemic trajectories of a stochastic SIRS model across three different resilience values: low, intermediate, and high. The relative prevalence was calculated by dividing infection prevalence by its mean value. (D) The heat map represents the intrinsic resilience of a system as a function of the basic reproduction number \mathcal{R}_0 and the duration of immunity. (E) The heat map represents the epidemic amplitude as a function of the basic reproduction number \mathcal{R}_0 and the duration of immunity. The epidemic amplitude corresponds to $(\max I - \min I)/(2\bar{I})$, where \bar{I} represents the mean prevalence. (F) The relationship between pathogen resilience and epidemic amplitude.

317 this study, we showed that pathogen re-emergence patterns following pandemic per-
 318 turbations can be characterized through the lens of ecological resilience. We showed
 319 that variation in pathogen resilience can be explained by the differences in suscepti-
 320 ble host dynamics, where faster replenishment of the susceptible pool corresponds to
 321 a more resilient host-pathogen system. Finally, we showed that pathogen resilience
 322 also determines the sensitivity to stochastic perturbations.

323 We analyzed case time series of common respiratory infections and norovirus
 324 infections from Canada, Hong Kong, Korea, and the US to estimate their resilience.
 325 Overall, we estimated the resilience of these pathogens to range from 0.4/year to
 326 1.8/year, which is 3–14 times more resilient than prevaccination measles. These
 327 resilience estimates indicate that common respiratory pathogens and norovirus likely
 328 exhibit faster susceptible replenishment and are therefore more persistent, indicating
 329 potential challenges in controlling these pathogens.

330 Based on our resilience estimates, we made phenomenological predictions about
 331 when each pathogen will return to their endemic cycles. For the most part, we

332 accurately predicted which pathogens should have already returned before the end
333 of 2024. However, there were few exceptions (i.e., norovirus in Hong Kong and
334 rhinovirus/enterovirus in the US), suggesting a possibility that these may have con-
335 verged to different endemic cycles compared to their pre-pandemic epidemic patterns.
336 These changes may reflect changes in surveillance or actual shift in the dynamics,
337 caused by permanent changes in behavior or population-level immunity. While it may
338 seem unlikely that permanent changes in behavior would only affect a few pathogens
339 and not others, we cannot rule out this possibility given heterogeneity in the age of
340 infection across different respiratory pathogens [19, 20]. Differences in the mode of
341 transmission between respiratory vs gastrointestinal pathogens may also contribute
342 to the differences in responses to pandemic perturbations. However, it is unclear
343 why norovirus dynamics in Korea seemed to have returned, whereas those in Hong
344 Kong have not.

345 For almost half of the pathogens we considered, we predicted that their return
346 to original epidemic patterns is imminent. We will need a few more years of data
347 to test whether these pathogens will eventually return to their original dynamics
348 or eventually converge to a different attractor. Overall, these observations echo
349 earlier studies that highlighted the long-lasting impact of pandemic perturbations
350 [8, 21, 22, 4].

351 We showed that susceptible host dynamics shape pathogen resilience, where faster
352 replenishment of the susceptible population causes the pathogen to be more resilient.
353 For simplicity, we focus on waning immunity and birth as the main drivers of the
354 susceptible host dynamics but other mechanisms can also contribute to the replen-
355 ishment of the susceptible population. In particular, pathogen evolution, especially
356 the emergence of antigenically novel strains, can cause effective waning of immunity
357 in the population; therefore, we hypothesize that faster rates of antigenic evolution
358 can also cause a pathogen to be more resilient. Future studies should explore the
359 relationship between the rate of evolution and resilience for antigenically evolving
360 pathogens.

361 Quantifying pathogen resilience also offers novel approaches to validating population-
362 level epidemiological models. So far, most of model validation in infectious disease
363 ecology is based on the ability of a model to reproduce the observed epidemic dy-
364 namics and to predict future dynamics [23, 24, 25, 26, 27]. However, many models
365 can perform similarly under these criteria. For example, two major RSV models
366 have been proposed to explain biennial epidemic patterns: (1) a stage- and age-
367 structured model that allows disease severity to vary with number of past infections
368 and age of infection [25] and (2) a pathogen-interaction model that accounts for cross
369 immunity between RSV and human metapneumovirus [24]. Since both models can
370 accurately reproduce the observed epidemic patterns, standard criteria for model
371 validation do not allow us to distinguish between these two models from population-
372 level data alone. Instead, it would be possible to measure the empirical resilience of
373 each model by simulating various perturbations and compare them to estimates of
374 empirical resilience from data, using pandemic perturbations as an opportunity.

375 There are several limitations to our work. First, we did not extensively explore
376 other approaches to reconstructing the attractor. Recent studies showed that more
377 sophisticated approaches, such as using non-uniform embedding, can provide more
378 robust reconstruction for noisy data [18]. In the context of causal inference, choices
379 about embedding can have major impact on the resulting inference [28]. Our re-
380 silience estimates are likely overly confident given a lack of uncertainties in attractor
381 reconstruction as well as the simplicity of our statistical framework. Nonetheless,
382 as illustrated in our sensitivity analyses, inferences about pathogen resilience in our
383 SIRS model appear to be robust to decisions about embedding lags and dimensions—
384 this is because tracking the rate at which the system approaches the attractor is
385 likely a much simpler problem than making inferences about causal directionality.
386 Short pre-pandemic time series also limit our ability to accurately reconstruct the
387 attractor and contribute to the crudeness of our resilience estimates; although this is
388 less likely a problem for respiratory pathogens that are strongly annual, our attrac-
389 tor reconstruction may be inaccurate for those exhibiting multi-annual cycles, such
390 as adenovirus in Hong Kong and Korea. Uncertainties in pathogen dynamics due
391 to changes in testing patterns further contribute to the curdeness of our resilience
392 estimates. Despite these limitations, our qualitative prediction that common respi-
393 ratory pathogens are more resilient than prevaccination measles is also likely to be
394 robust, given how rapid many respiratory pathogens returned to their original cycles
395 following pandemic perturbations.

396 Predicting the impact of anthropogenic changes on infectious disease dynamics
397 is a fundamental aim of infectious disease research in a rapidly changing world. Our
398 study illustrates that how a host-pathogen system responds to both small and large
399 perturbations is largely predictable through the lens of ecological resilience. In par-
400 ticular, quantifying the resilience of a host-pathogen system offers a unique insight
401 into questions about endemic pathogens' responses to pandemic perturbations, in-
402 cluding whether some pathogens will exhibit long-lasting impact from the pandemic
403 perturbation or not. More broadly, a detailed understanding of the determinants of
404 pathogen resilience can provide deeper understanding of pathogen persistence.

405 Materials and Methods

406 Data

407 We gathered time series on respiratory infections from Canada, Hong Kong, Korea,
408 and United States (US). As a reference, we also included time series data on norovirus
409 infections for available countries. In contrast to respiratory pathogens, we expect
410 gastrointestinal viruses, such as norovirus, to be differently affected by pandemic
411 perturbations.

412 Weekly time series of respiratory infection cases in Canada comes from a pub-
413 licly available website by the Respiratory Virus Detection Surveillance System, which
414 collect data from select laboratories across Canada [29]. Weekly time series of respi-

415 respiratory infection cases in Hong Kong comes from a publicly available website by the
416 Centre for Health Protection, Department of Health [30, 31]. Weekly time series of
417 acute respiratory infection cases in Korea comes from a publicly available website by
418 the Korea Disease Control and Prevention Agency [32]. Finally, weekly time series
419 of respiratory infection cases in the US were obtained from the National Respiratory
420 and Enteric Virus Surveillance System. Time series on number of tests were also
421 available in Canada, Hong Kong, and the US, but not in Korea. **[SWP: Not sure**
422 **how to cite NREVSS data because we got it by emailing them...]**

423 Data processing

424 For all time series, we rounded every year to 52 weeks by taking the average number
425 of cases and tests between the 52nd and 53rd week. We also rescale all time series to
426 account for changes in testing patterns, which are then used for the actual analysis.

427 For Canada, an increase in testing was observed from 2013 to 2024 (Supplementary
428 Figure S15). To account for this increase, we calculated a 2 year moving average
429 for the number of tests for each pathogen, which we used as a proxy for testing effort.
430 Then, we divided the smoothed testing patterns by the smoothed value at the final
431 week such that the testing effort has a maximum of 1. We then divided weekly cases
432 by the testing effort to obtain a scaled case time series. A similar approach was used
433 earlier for an analysis of RSV time series in the US to account for changes in testing
434 patterns [25].

435 For Hong Kong, we also applied the same scaling procedure to the time series
436 as we did for Canada. In this case, we only adjusted for testing efforts up to the
437 end of 2019 because there was a major reduction in testing for common respiratory
438 pathogens since 2020 (Supplementary Figure S16).

439 For Korea, while we did not have information on testing, the reported number
440 of respiratory infections consistently increased from 2013 to the end of 2019, which
441 we interpreted as changes in testing patterns (Supplementary Figure S17). Since
442 we did not have testing numbers, we used the weekly sum of all acute respiratory
443 viral infection cases as a proxy for testing, which were further smoothed with moving
444 averaged and scaled to have a maximum of 1. For Korea, we also only adjusted for
445 testing efforts up to the end of 2019.

446 In the US, there has been a large increase in testing against some respiratory
447 pathogens, especially RSV, which could not be corrected for through simple scaling
448 (Supplementary Figure S18). Instead, we derived an incidence proxy by multiplying
449 the test positivity with influenza-like illness positivity, which was taken from
450 <https://gis.cdc.gov/grasp/fluview/fluportaldashboard.html>. This method
451 of estimating an incidence proxy has been recently applied in the analysis of seasonal
452 coronaviruses [7] and *Mycoplasma pneumoniae* infections [4]. Detailed assumptions
453 and justifications are provided in [33].

454 **Data summary**

455 To make qualitative comparisons between pre- and post-perturbation dynamics of
456 respiratory pathogen circulation patterns, we calculate the mean seasonal patterns
457 using time series of either rescaled cases or incidence proxy estimates before 2020. We
458 do so by taking the mean value in each week across all years before 2020. Confidence
459 intervals around the means are calculated using a simple t test.

460 **Estimating pathogen resilience**

461 In order to measure pathogen resilience from surveillance data, we first reconstructed
462 the empirical pre-pandemic attractor of the system using Takens' embedding theorem
463 [14]. Specifically, for a given pathogen, we took the pre-pandemic (before 2020)
464 case time series $C(t)$ and reconstruct the attractor using delayed embedding with a
465 uniform delay of τ and dimension M :

$$X_{\tau,m}(t) = \langle \log(C(t) + 1), \log(C(t - \tau) + 1), \dots, \log(C(t - (M - 1)\tau) + 1) \rangle. \quad (2)$$

466 Here, the delay τ was determined by calculating the autocorrelation of the logged
467 pre-pandemic time series and asking when the autocorrelation crosses 0 for the first
468 time [18]; a typical delay for an annual outbreak is around 13 weeks.

469 Then, for a given delay τ , we determined the embedding dimension M using the
470 false nearest neighbors approach [17, 18]. To do so, we started with an embedding
471 dimension e and construct a set of points $A_{\tau,e} = \{X_{\tau,e}(t) | t < 2020\}$. Then, for
472 each point $X_{\tau,e}(t)$, we determined the nearest neighbor from the set $A_{\tau,e}$, which we
473 denote $X_{\tau,e}(t_{nn})$ for $t \neq t_{nn}$. Then, if the distance between these two points on $e + 1$
474 dimension, $D_{\tau,e+1}(t) = \|X_{\tau,e+1}(t_{nn}) - X_{\tau,e+1}(t)\|_2$, is larger than their distance on
475 e dimension, $D_{\tau,e}(t) = \|X_{\tau,e}(t_{nn}) - X_{\tau,e}(t)\|_2$, these two points are deemed to be
476 false nearest neighbors; specifically, we used a threshold R for the ratio between
477 two distances $D_{\tau,e+1}(t)/D_{\tau,e}(t)$ to determine false nearest neighbors. For the main
478 analysis, we used $R = 10$, which was chosen from a sensitivity analysis against
479 simulated data (Supplementary Text). Once we determined the embedding lag τ
480 and dimension M , we apply the embedding to the entire time series and calculate
481 the nearest neighbor distance against the attractor $A_{\tau,M}$ to obtain a time series of
482 distance from the attractor $D_{\tau,M}(t)$.

483 From a time series of distances from the attractor, we estimated pathogen re-
484 silience by fitting a linear regression to an appropriate window. To automatically se-
485 lect the fitting window, we began by smoothing the distance time series using locally
486 estimated scatterplot smoothing (LOESS) to obtain $\hat{D}_{\tau,M}(t)$, where the smoothing
487 is performed on a log scale and exponentiated afterwards. Then, we determined
488 threshold values (T_{start} and T_{end}) for the smoothed distances and choose the fitting
489 window based on when $\hat{D}_{\tau,M}(t)$ crosses these threshold values for the first time.
490 These thresholds were determined by first calculating maximum distance,

$$\max \hat{D} = \max \hat{D}_{\tau,M}(t), \quad (3)$$

⁴⁹¹ and mean pre-pandemic distance,

$$\hat{D}_{\text{mean}} = \frac{1}{N_{t < 2020}} \sum_{t < 2020} \hat{D}_{\tau, M}(t), \quad (4)$$

⁴⁹² as a reference, and then dividing their ratios into K equal bins:

$$T_{\text{start}} = \hat{D}_{\text{mean}} \times \left(\frac{\max \hat{D}}{\hat{D}_{\text{mean}}} \right)^{(K-a)/K} \quad (5)$$

$$T_{\text{end}} = \hat{D}_{\text{mean}} \times \left(\frac{\max \hat{D}}{\hat{D}_{\text{mean}}} \right)^{a/K} \quad (6)$$

⁴⁹³ where a represents the truncation threshold. This allows us to discard the initial
⁴⁹⁴ period during which the distance increases (from the introduction of intervention
⁴⁹⁵ measures) and the final period during which the distance plateaus (as the system
⁴⁹⁶ reaches an attractor). The fitting window is determined based on when the smoothed
⁴⁹⁷ distance $\hat{D}_{\tau, M}(t)$ crosses these threshold values for the first time; then, we fit a
⁴⁹⁸ linear regression to logged (unsmoothed) distances $\log D_{\tau, M}(t)$ using that window.
⁴⁹⁹ Alongside the threshold R for the false nearest neighbors approach, we tested optimal
⁵⁰⁰ choices for K and a values using simulations (Supplementary Text). We used $K = 19$
⁵⁰¹ and $a = 2$ throughout the paper based on the simulation results.

⁵⁰² Mathematical modeling

⁵⁰³ Throughout the paper, we use a series of mathematical models to illustrate the
⁵⁰⁴ concept of pathogen resilience and to understand the determinants of pathogen re-
⁵⁰⁵ silience. In general, the intrinsic resilience for a given system is given by the largest
⁵⁰⁶ real part of the eigenvalues of the linearized system at endemic equilibrium. Here, we
⁵⁰⁷ focus on the SIRS model with demography (birth and death) and present the details
⁵⁰⁸ of other models in Supplementary Text. The SIRS (Susceptible-Infected-Recovered-
⁵⁰⁹ Susceptible) model is the simplest model that allows for waning of immunity, where
⁵¹⁰ recovered (immune) individuals are assumed to become fully susceptible after an
⁵¹¹ average of $1/\delta$ time period. The dynamics of the SIRS model is described by the
⁵¹² following set of differential equations:

$$\frac{dS}{dt} = \mu - \beta(t)SI - \mu S + \delta R \quad (7)$$

$$\frac{dI}{dt} = \beta(t)SI - (\gamma + \mu)I \quad (8)$$

$$\frac{dR}{dt} = \gamma I - (\delta + \mu)R \quad (9)$$

$$(10)$$

513 where μ represents the birth/death rate, $\beta(t)$ represents the time-varying transmission rate, and γ represents the recovery rate. The basic reproduction number
 514 $\mathcal{R}_0(t) = \beta(t)/(\gamma + \mu)$ is defined as the average number of secondary infections that
 515 a single infected individual would cause in a fully susceptible population at time t
 516 and measures the intrinsic transmissibility of a pathogen.

518 When we first introduced the idea of pathogen resilience (Figure 2), we imposed
 519 sinusoidal changes to the transmission rate to account for seasonal transmission:

$$\beta(t) = b_1(1 + \theta \cos(2\pi(t - \phi)))\alpha(t), \quad (11)$$

520 where b_1 represents the baseline transmission rate, θ represents the seasonal amplitude,
 521 and ϕ represents the seasonal offset term. Here, we also introduced an extra
 522 multiplicative term $\alpha(t)$ to account for the impact of pandemic perturbations, where
 523 $\alpha(t) < 1$ indicates transmission reduction. Figure 2A and 2B were generated assuming
 524 $b_1 = 3 \times (365/7 + 1/50)/\text{years}$, $\theta = 0.2$, $\phi = 0$, $\mu = 1/50/\text{years}$, $\gamma = 365/7/\text{years}$,
 525 and $\delta = 1/2/\text{years}$. In Figure 2A, we imposed a 50% transmission reduction for 6
 526 months from 2020:

$$\alpha(t) = \begin{cases} 0.5 & 2020 \leq t < 2020.5 \\ 1 & \text{otherwise} \end{cases} \quad (12)$$

527 In Figure 2B, we imposed a 50% transmission reduction for 6 months from 2020 and
 528 a permanent 10% reduction onward:

$$\alpha(t) = \begin{cases} 1 & t < 2020 \\ 0.5 & 2020 \leq t < 2020.5 \\ 0.9 & 2020.5 \leq t \end{cases} \quad (13)$$

529 In both scenarios, we simulated the SIRS model from the following initial conditions
 530 ($S(0) = 1/\mathcal{R}_0$, $I(0) = 1 \times 10^{-6}$, and $R(0) = 1 - S(0) - I(0)$) from 1900 until 2030.

531 To measure the empirical resilience of the SIRS model (Figure 2C and 2F), we
 532 computed the normalized distance between post-intervention susceptible and logged
 533 infected proportions and their corresponding unperturbed values at the same time:

$$\sqrt{\left(\frac{S(t) - S_{\text{unperturbed}}(t)}{\sigma_S}\right)^2 + \left(\frac{\log I(t) - \log I_{\text{unperturbed}}(t)}{\sigma_{\log I}}\right)^2}, \quad (14)$$

534 where σ_S and $\sigma_{\log I}$ represent the standard deviation in the unperturbed susceptible
 535 and logged infected proportions. The unperturbed values were obtained by simulating
 536 the same SIRS model without pandemic perturbations ($\alpha = 1$). We normalized
 537 the differences in susceptible and logged infected proportions to allow both quantities
 538 to equally contribute to the changes in distance from the attractor. We used logged
 539 prevalence, instead of absolute prevalence, in order to capture epidemic dynamics
 540 in deep troughs during the intervention period. In Supplementary Materials, we
 541 also compared how the degree of seasonal transmission affects empirical resilience

542 by varying θ from 0 to 0.4; when we assumed no seasonality ($\theta = 0$), we did not
543 normalize the distance because the standard deviation of pre-intervention dynamics
544 are zero.

545 We used the SIRS model to understand how underlying epidemiological parameters
546 affect pathogen resilience and link this relationship to underlying susceptible
547 host dynamics. For the simple SIRS model without seasonal transmission ($\theta = 0$),
548 the intrinsic resilience corresponds to

$$-\frac{\text{Re}(\lambda)}{2} = \frac{\delta + \beta I^* + \mu}{2}. \quad (15)$$

549 Here, I^* represents the prevalence at endemic equilibrium:

$$I^* = \frac{(\delta + \mu)(\beta - (\gamma + \mu))}{\beta(\delta + \gamma + \mu)}. \quad (16)$$

550 The susceptible replenishment rate is given by

$$S_{\text{replenish}} = \frac{\mu + \delta R}{S^*}, \quad (17)$$

551 where $S^* = 1/\mathcal{R}_0$ represents the equilibrium proportion of susceptible individuals.
552 We varied the basic reproduction number \mathcal{R}_0 between 1.1 to 6 and the average
553 duration of immunity $1/\delta$ between 2 to 4 years, and computed these two quantities.
554 In doing so, we fixed all other parameters: $\mu = 1/80/\text{years}$ and $\gamma = 365/7/\text{years}$.

555 Finally, we used a seasonally unforced stochastic SIRS model without demog-
556 raphy to understand how pathogen resilience affects sensitivity of the system to
557 demographic stochasticity (see Supplementary Text for the details of the stochastic
558 SIRS model). By varying the basic reproduction number \mathcal{R}_0 between 2 to 20 and
559 the average duration of immunity $1/\delta$ between 1 to 40 years, we ran the the SIRS
560 model for 100 years and computed the epidemic amplitude, which we defined as
561 $(\max I - \min I)/(2\bar{I})$. Each simulation began from the equilibrium, and we trun-
562 cated initial 25 years before computing the epidemic amplitude. In doing so, we
563 assumed $\gamma = 365/7/\text{years}$ and fixed the population size to 1 billion to prevent any
564 fadeouts. We also considered using a seasonally forced stochastic SIRS model with-
565 out demography, assuming an amplitude of seasonal forcing of 0.04; in this case,
566 we computed the relative epidemic amplitude by comparing the deterministic and
567 stochastic trajectories (Supplementary Materials).

568 Data availability

569 All data and code are stored in a publicly available GitHub repository (<https://github.com/cobeylab/return-time>).

⁵⁷¹ **Funding**

⁵⁷² S.W.P. is a Peter and Carmen Lucia Buck Foundation Awardee of the Life Sciences
⁵⁷³ Research Foundation.

574 **Supplementary Text**

575 **Resilience of a stage-structured system.**

576 In Figure 2G–I, we used a more realistic, stage-structured model to illustrate how
 577 transient phenomena can cause the system to slow down. Specifically, we used the
 578 stage-structured RSV model proposed by [25], which assumes that subsequent rein-
 579 fections cause an individual to become less susceptible and transmissible than previ-
 580 ous infections. The model dynamics can be described as follows:

$$\frac{dM}{dt} = \mu - (\omega + \mu)M \quad (S1)$$

$$\frac{dS_0}{dt} = \omega M - (\lambda(t) + \mu)S_0 \quad (S2)$$

$$\frac{dI_1}{dt} = \lambda(t)S_0 - (\gamma_1 + \mu)I_1 \quad (S3)$$

$$\frac{dS_1}{dt} = \gamma_1 I_1 - (\sigma_1 \lambda(t) + \mu)S_1 \quad (S4)$$

$$\frac{dI_2}{dt} = \sigma_1 \lambda(t)S_1 - (\gamma_2 + \mu)I_2 \quad (S5)$$

$$\frac{dS_2}{dt} = \gamma_2 I_2 - (\sigma_2 \lambda(t) + \mu)S_2 \quad (S6)$$

$$\frac{dI_3}{dt} = \sigma_2 \lambda(t)S_2 - (\gamma_3 + \mu)I_3 \quad (S7)$$

$$\frac{dS_3}{dt} = \gamma_3 I_3 - (\sigma_3 \lambda(t) + \mu)S_3 + \gamma_4 I_4 \quad (S8)$$

$$\frac{dI_4}{dt} = \sigma_3 \lambda(t)S_3 - (\gamma_4 + \mu)I_4 \quad (S9)$$

(S10)

581 where M represents the proportion of individuals who are maternally immune; S_i
 582 represents the proportion of individuals who are susceptible after i prior infections; I_i
 583 represents the proportion of individuals who are currently (re)-infected with their i -th
 584 infection; μ represents the birth and death rates; $1/\omega$ represents the mean duration
 585 of maternal immunity; $1/\gamma_i$ represents the mean duration of infection; $\lambda(t)$ represents
 586 the force of infection; and σ_i represents the reduction in susceptibility for the i -th
 587 reinfection. The force of infection is modeled using a sinusoidal function:

$$\beta(t) = b_1(1 + \theta \cos(2\pi(t - \phi)))\alpha(t) \quad (S11)$$

$$\lambda(t) = \beta(I_1 + \rho_1 I_2 + \rho_2(I_3 + I_4)), \quad (S12)$$

588 where b_1 represents the baseline transmission rate; θ represents the seasonal ampli-
 589 tude; ϕ represents the seasonal offset term; $\alpha(t)$ represents the intervention effect;
 590 and ρ_i represents the impact of immunity on transmission reduction. We used the

591 following parameters to simulate the impact of interventions on epidemic dynam-
 592 ics [25]: $b_1 = 9 \times (365/10 + 1/80)/\text{years}$, $\theta = 0.2$, $\phi = -0.1$, $\omega = 365/112/\text{years}$,
 593 $\gamma_1 = 365/10/\text{years}$, $\gamma_2 = 365/7/\text{years}$, $\gamma_3 = 365/5/\text{years}$, $\sigma_1 = 0.76$, $\sigma_2 = 0.6$,
 594 $\sigma_3 = 0.4$, $\rho_1 = 0.75$, $\rho_2 = 0.51$, and $\mu = 1/80/\text{years}$. We assumed a 50% transmis-
 595 sion reduction for 6 months from 2020:

$$\alpha(t) = \begin{cases} 0.5 & 2020 \leq t < 2020.5 \\ 1 & \text{otherwise} \end{cases} \quad (\text{S13})$$

596 The model was simulated from 1900 to 2030 using the following initial conditions:
 597 $M = 0$, $S_0 = 1/\mathcal{R}_0 - I_1$, $I_1 = 1 \times 10^{-6}$, $S_1 = 1 - 1/\mathcal{R}_0$, $I_2 = 0$, $S_2 = 0$, $I_3 = 0$,
 598 $S_3 = 0$, and $I_4 = 0$. For the phase plane analysis (Figure 2H) and distance analysis
 599 (Figure 2I), we relied on the average susceptibility,

$$\bar{S} = S_0 + \sigma_1 S_1 + \sigma_2 S_2 + \sigma_3 S_3, \quad (\text{S14})$$

600 and total prevalence,

$$I_{\text{total}} = I_1 + I_2 + I_3 + I_4. \quad (\text{S15})$$

601 These quantities were used to compute the normalized distance from the attractor,
 602 as described in the main text.

603 Resilience of a multistrain system.

604 We used a simple two-strain model to show that a multistrain host-pathogen system
 605 that is coupled through cross immunity can be described by a single resilience value.
 606 The model dynamics can be described as follows [24]:

$$\frac{dS}{dt} = \mu - \mu S - (\lambda_1 + \lambda_2)S + \rho_1 R_1 + \rho_2 R_2 \quad (\text{S16})$$

$$\frac{dI_1}{dt} = \lambda_1 S - (\gamma_1 + \mu)I_1 \quad (\text{S17})$$

$$\frac{dI_2}{dt} = \lambda_2 S - (\gamma_2 + \mu)I_2 \quad (\text{S18})$$

$$\frac{dR_1}{dt} = \gamma_1 I_1 - \lambda_2 \epsilon_{21} R_1 - \rho_1 R_1 + \rho_2 R - \mu R_1 \quad (\text{S19})$$

$$\frac{dR_2}{dt} = \gamma_2 I_2 - \lambda_1 \epsilon_{12} R_2 - \rho_2 R_2 + \rho_1 R - \mu R_2 \quad (\text{S20})$$

$$\frac{dJ_1}{dt} = \lambda_1 \epsilon_{12} R_2 - (\gamma_1 + \mu)J_1 \quad (\text{S21})$$

$$\frac{dJ_2}{dt} = \lambda_2 \epsilon_{21} R_1 - (\gamma_2 + \mu)J_2 \quad (\text{S22})$$

$$\frac{dR}{dt} = \gamma_1 J_1 + \gamma_2 J_2 - \rho_1 R - \rho_2 R - \mu R \quad (\text{S23})$$

where S represents the proportion of individuals who are fully susceptible to infections by both strains; I_1 represents the proportion of individuals who are infected with strain 1 without prior immunity; I_2 represents the proportion of individuals who are infected with strain 2 without prior immunity; R_1 represents the proportion of individuals who are fully immune against strain 1 and partially susceptible to reinfection by strain 2; R_2 represents the proportion of individuals who are fully immune against strain 2 and partially susceptible to reinfection by strain 1; J_1 represents the proportion of individuals who are infected with strain 1 with prior immunity against strain 2; J_2 represents the proportion of individuals who are infected with strain 2 with prior immunity against strain 1; R represents the proportion of individuals who are immune to infections from both strains; μ represents the birth/death rate; λ_1 and λ_2 represent the force of infection from strains 1 and 2, respectively; ρ_1 and ρ_2 represent the waning immunity rate; γ_1 and γ_2 represent the recovery rate; ϵ_{12} and ϵ_{21} represent the susceptibility to reinfection with strains 2 and 1, respectively, given prior immunity from infection with strains 1 and 2, respectively. The force of infection is modeled as follows:

$$\beta_1 = b_1(1 + \theta_1 \sin(2\pi(t - \phi_1)))\alpha(t) \quad (\text{S24})$$

$$\beta_2 = b_2(1 + \theta_2 \sin(2\pi(t - \phi_2)))\alpha(t) \quad (\text{S25})$$

$$\lambda_1 = \beta_1(I_1 + J_1) \quad (\text{S26})$$

$$\lambda_2 = \beta_2(I_2 + J_2) \quad (\text{S27})$$

In Supplementary Figures S2–S4, we assumed the following parameters: $b_1 = 2 \times 52/\text{years}$, $b_2 = 4 \times 52/\text{years}$, $\phi_1 = \phi_2 = 0$, $\epsilon_{12} = 0.9$, $\epsilon_{21} = 0.5$, $\gamma_1 = \gamma_2 = 52/\text{years}$, $\rho_1 = \rho_2 = 1/\text{years}$, and $\mu = 1/70/\text{years}$. For all simulations, we assumed a 50% transmission reduction for 6 months from 2020:

$$\alpha(t) = \begin{cases} 0.5 & 2020 \leq t < 2020.5 \\ 1 & \text{otherwise} \end{cases} \quad (\text{S28})$$

The seasonal amplitude θ is varied from 0 to 0.4. All simulations were ran from 1900 to 2030 with following initial conditions: $S(0) = 1 - 2 \times 10^{-6}$, $I_1(0) = 1 \times 10^{-6}$, $I_2(0) = 1 \times 10^{-6}$, $R_1(0) = 0$, $R_2(0) = 0$, $J_1(0) = 0$, $J_2(0) = 0$, and $R(0) = 0$.

We considered three scenarios for measuring pathogen resilience: (1) we only have information about strain 1, (2) we only have information about strain 2, and (3) we are unable to distinguish between strains. In the first two scenarios (see panels A–C for strain 1 and panels D–F for strain 2), we considered the dynamics of average susceptibility for each strain and total prevalence:

$$\bar{S}_1 = S + \epsilon_{12}R_2 \quad (\text{S29})$$

$$\hat{I}_1 = I_1 + J_1 \quad (\text{S30})$$

$$\bar{S}_2 = S + \epsilon_{21}R_1 \quad (\text{S31})$$

$$\hat{I}_2 = I_2 + J_2 \quad (\text{S32})$$

635 In the third scenario (panels G–I), we considered the dynamics of total susceptible
636 and infected populations:

$$\hat{S} = S + R_2 + R_1 \quad (\text{S33})$$

$$\hat{I} = I_1 + J_1 + I_2 + J_2 \quad (\text{S34})$$

637 These quantities were used to compute the normalized distance from the attractor,
638 as described in the main text.

639 Estimating intrinsic resilience using mechanistic model

640 We tested whether we can reliably estimate the intrinsic resilience of a system by fit-
641 ting a mechanistic model. Specifically, we simulated case time series from stochastic
642 SIRS and two-strain models and fitted a simple, deterministic SIRS model using a
643 Bayesian framework.

644 We simulated the models in discrete time with a daily time step ($\Delta t = 1$),
645 incorporating demographic stochasticity:

$$\beta(t) = \mathcal{R}_0 \left(1 + \theta \cos \left(\frac{2\pi t}{364} \right) \right) \alpha(t)(1 - \exp(-\gamma)) \quad (\text{S35})$$

$$\text{FOI}(t) = \beta(t)I(t - \Delta t)/N \quad (\text{S36})$$

$$B(t) \sim \text{Poisson}(\mu N) \quad (\text{S37})$$

$$\Delta S(t) \sim \text{Binom}(S(t - \Delta t), 1 - \exp(-(\text{FOI}(t) + \mu)\Delta t)) \quad (\text{S38})$$

$$N_{SI}(t) \sim \text{Binom}\left(\Delta S(t), \frac{\text{FOI}(t)}{\text{FOI}(t) + \mu}\right) \quad (\text{S39})$$

$$\Delta I(t) \sim \text{Binom}(I(t - \Delta t), 1 - \exp(-(\gamma + \mu)\Delta t)) \quad (\text{S40})$$

$$N_{IR}(t) \sim \text{Binom}\left(\Delta I(t), \frac{\gamma}{\gamma + \mu}\right) \quad (\text{S41})$$

$$\Delta R(t) \sim \text{Binom}(R(t - \Delta t), 1 - \exp(-(\delta + \mu)\Delta t)) \quad (\text{S42})$$

$$N_{RS}(t) \sim \text{Binom}\left(\Delta R(t), \frac{\delta}{\delta + \mu}\right) \quad (\text{S43})$$

$$S(t) = S(t - \Delta t) + N_{RS}(t) + B(t) - \Delta S(t) \quad (\text{S44})$$

$$I(t) = I(t - \Delta t) + N_{SI}(t) - \Delta I(t) \quad (\text{S45})$$

$$R(t) = R(t - \Delta t) + N_{IR}(t) - \Delta R(t) \quad (\text{S46})$$

646 where FOI represent the force of infection; N_{ij} represent the number of individuals
647 moving from compartment i to j on a given day; and $B(t)$ represents the number
648 of new births. We simulated the model on a daily scale—assuming 364 days in a
649 year so that it can be evenly grouped into 52 weeks—with the following parameters:
650 $\mathcal{R}_0 = 3$, $\theta = 0.1$, $\gamma = 1/7/\text{days}$, $\delta = 1/(364 \times 2)/\text{days}$, $\mu = 1/(364 \times 50)/\text{days}$, and
651 $N = 1 \times 10^8$. The model was simulated from 1900 to 2030 assuming $S(0) = N/3$,

652 $I(0) = 100$, and $R(0) = N - S(0) - I(0)$. The observed incidence from the model
653 was then simulated as follows:

$$C(t) = \text{Beta-Binom}(N_{SI}(t), \rho, k), \quad (\text{S47})$$

654 where ρ represents the reporting probability and k represents the overdispersion
655 parameter of beta-binomial distribution. Here, we used the beta-binomial distribution
656 to account for overdispersion in reporting. We assumed $\rho = 0.002$ (i.e., 0.2%
657 probability) and $k = 1000$.

658 We used an analogous approach for the two-strain model:

$$\beta_1(t) = b_1 \left(1 + \theta_1 \cos \left(\frac{2\pi(t - \phi_1)}{364} \right) \right) \alpha(t) \quad (\text{S48})$$

$$\beta_2(t) = b_2 \left(1 + \theta_2 \cos \left(\frac{2\pi(t - \phi_2)}{364} \right) \right) \alpha(t) \quad (\text{S49})$$

$$\text{FOI}_1(t) = \beta_1(t)(I_1(t - \Delta t) + J_1(t - \Delta t))/N \quad (\text{S50})$$

$$\text{FOI}_2(t) = \beta_2(t)(I_2(t - \Delta t) + J_2(t - \Delta t))/N \quad (\text{S51})$$

$$B(t) \sim \text{Poisson}(\mu N) \quad (\text{S52})$$

$$\Delta S(t) \sim \text{Binom}(S(t - \Delta t), 1 - \exp(-(\text{FOI}_1(t) + \text{FOI}_2(t) + \mu)\Delta t)) \quad (\text{S53})$$

$$N_{SI_1}(t) \sim \text{Binom}\left(\Delta S(t), \frac{\text{FOI}_1(t)}{\text{FOI}_1(t) + \text{FOI}_2(t) + \mu}\right) \quad (\text{S54})$$

$$N_{SI_2}(t) \sim \text{Binom}\left(\Delta S(t), \frac{\text{FOI}_2(t)}{\text{FOI}_1(t) + \text{FOI}_2(t) + \mu}\right) \quad (\text{S55})$$

$$\Delta I_1(t) \sim \text{Binom}(I_1(t - \Delta t), 1 - \exp(-(\gamma_1 + \mu)\Delta t)) \quad (\text{S56})$$

$$N_{I_1 R_1}(t) \sim \text{Binom}\left(\Delta I_1(t), \frac{\gamma_1}{\gamma_1 + \mu}\right) \quad (\text{S57})$$

$$\Delta I_2(t) \sim \text{Binom}(I_2(t - \Delta t), 1 - \exp(-(\gamma_2 + \mu)\Delta t)) \quad (\text{S58})$$

$$N_{I_2 R_2}(t) \sim \text{Binom}\left(\Delta I_2(t), \frac{\gamma_2}{\gamma_2 + \mu}\right) \quad (\text{S59})$$

$$\Delta R_1(t) \sim \text{Binom}(R_1(t - \Delta t), 1 - \exp(-(\epsilon_{21}\text{FOI}_2(t) + \rho_1 + \mu)\Delta t)) \quad (\text{S60})$$

$$N_{R_1 S}(t) \sim \text{Binom}\left(\Delta R_1(t), \frac{\rho_1}{\epsilon_{21}\text{FOI}_2(t) + \rho_1 + \mu}\right) \quad (\text{S61})$$

$$N_{R_1 J_2}(t) \sim \text{Binom}\left(\Delta R_1(t), \frac{\epsilon_{21}\text{FOI}_2(t)}{\epsilon_{21}\text{FOI}_2(t) + \rho_1 + \mu}\right) \quad (\text{S62})$$

$$\Delta R_2(t) \sim \text{Binom}(R_2(t - \Delta t), 1 - \exp(-(\epsilon_{12}\text{FOI}_1(t) + \rho_2 + \mu)\Delta t)) \quad (\text{S63})$$

$$N_{R_2 S}(t) \sim \text{Binom}\left(\Delta R_2(t), \frac{\rho_2}{\epsilon_{12}\text{FOI}_1(t) + \rho_2 + \mu}\right) \quad (\text{S64})$$

$$N_{R_2 J_1}(t) \sim \text{Binom}\left(\Delta R_2(t), \frac{\epsilon_{12}\text{FOI}_1(t)}{\epsilon_{12}\text{FOI}_1(t) + \rho_2 + \mu}\right) \quad (\text{S65})$$

$$\Delta J_1(t) \sim \text{Binom}(J_1(t - \Delta t), 1 - \exp(-(\gamma_1 + \mu)\Delta t)) \quad (\text{S66})$$

$$N_{J_1R}(t) \sim \text{Binom}\left(\Delta J_1(t), \frac{\gamma_1}{\gamma_1 + \mu}\right) \quad (\text{S67})$$

$$\Delta J_2(t) \sim \text{Binom}(J_2(t - \Delta t), 1 - \exp(-(\gamma_2 + \mu)\Delta t)) \quad (\text{S68})$$

$$N_{J_2R}(t) \sim \text{Binom}\left(\Delta J_2(t), \frac{\gamma_2}{\gamma_2 + \mu}\right) \quad (\text{S69})$$

$$\Delta R(t) \sim \text{Binom}(R(t - \Delta t), 1 - \exp(-(\rho_1 + \rho_2 + \mu)\Delta t)) \quad (\text{S70})$$

$$N_{RR_1}(t) \sim \text{Binom}\left(\Delta R(t), \frac{\rho_1}{\rho_1 + \rho_2 + \mu}\right) \quad (\text{S71})$$

$$N_{RR_2}(t) \sim \text{Binom}\left(\Delta R(t), \frac{\rho_2}{\rho_1 + \rho_2 + \mu}\right) \quad (\text{S72})$$

$$S(t) = S(t - \Delta t) - \Delta S(t) + B(t) + N_{R_1S}(t) + N_{R_2S}(t) \quad (\text{S73})$$

$$I_1(t) = I_1(t - \Delta t) - \Delta I_1(t) + N_{SI_1}(t) \quad (\text{S74})$$

$$I_2(t) = I_2(t - \Delta t) - \Delta I_2(t) + N_{SI_2}(t) \quad (\text{S75})$$

$$R_1(t) = R_1(t - \Delta t) - \Delta R_1(t) + N_{I_1R_1}(t) + N_{RR_1}(t) \quad (\text{S76})$$

$$R_2(t) = R_2(t - \Delta t) - \Delta R_2(t) + N_{I_2R_2}(t) + N_{RR_2}(t) \quad (\text{S77})$$

$$J_1(t) = J_1(t - \Delta t) - \Delta J_1(t) + N_{R_2J_1}(t) \quad (\text{S78})$$

$$J_2(t) = J_2(t - \Delta t) - \Delta J_2(t) + N_{R_1J_2}(t) \quad (\text{S79})$$

$$R(t) = R(t - \Delta t) - \Delta R(t) + N_{J_1R}(t) + N_{J_2R}(t) \quad (\text{S80})$$

We simulated the model on a daily scale with previously estimated parameters for the RSV-HMPV interaction [24]: $b_1 = 1.7/\text{weeks}$, $b_2 = 1.95/\text{weeks}$, $\theta_1 = 0.4$, $\theta_2 = 0.3$, $\phi_1 = 0.005 \times 7/364$, $\phi_2 = 4.99 \times 7/364$, $\epsilon_{12} = 0.92$, $\epsilon_{21} = 0.45$, $\gamma_1 = 1/10/\text{days}$, $\gamma_2 = 1/10/\text{days}$, $\rho_1 = 1/364/\text{days}$, $\rho_2 = 1/364/\text{days}$, $\mu = 1/(70 \times 364)/\text{days}$, and $N = 1 \times 10^8$. The model was simulated from 1900 to 2030 assuming $S(0) = N - 200$, $I_1(0) = 100$, $I_2(0) = 100$, $R_1(0) = 0$, $R_2(0) = 0$, $J_1(0) = 0$, $J_2(0) = 0$, and $R(0) = 0$. The observed incidence for each strain is then simulated as follows:

$$C_1(t) = \text{Beta-Binom}(N_{SI_1}(t) + N_{R_2J_1}, \rho, k), \quad (\text{S81})$$

$$C_2(t) = \text{Beta-Binom}(N_{SI_2}(t) + N_{R_1J_2}, \rho, k), \quad (\text{S82})$$

where ρ represents the reporting probability and k represents the overdispersion parameter of beta-binomial distribution. We assumed $\rho = 0.002$ (i.e., 0.2% probability) and $k = 500$. We also considered the total incidence: $C_{\text{total}}(t) = C_1(t) + C_2(t)$.

For both models, we considered a more realistically shaped pandemic perturbation $\alpha(t)$ to challenge our ability to estimate the intervention effects. Thus, we assumed a 40% transmission reduction for 3 months from March 2020, followed by a 10% transmission reduction for 6 months, 20% transmission reduction for 3 months,

673 and a final return to normal levels:

$$\alpha(t) = \begin{cases} 1 & t < 2020.25 \\ 0.6 & 2020.25 \leq t < 2020.5 \\ 0.9 & 2020.5 \leq t < 2021 \\ 0.8 & 2021 \leq t < 2021.25 \\ 1 & 2021.25 \leq t \end{cases}. \quad (\text{S83})$$

674 For all simulations, we truncated the time series from the beginning of 2014 to the
675 end of 2023 and aggregate them into weekly cases.

676 To infer intrinsic resilience from time series, we fitted a simple discrete time,
677 deterministic SIRS model [4]:

$$\Delta t = 1 \text{ week} \quad (\text{S84})$$

$$\text{FOI}(t) = \beta(t)(I(t - \Delta t) + \omega)/N \quad (\text{S85})$$

$$\Delta S(t) = [1 - \exp(-(\text{FOI}(t) + \mu)\Delta t)] S(t - \Delta t) \quad (\text{S86})$$

$$N_{SI}(t) = \frac{\text{FOI}(t)\Delta S(t)}{\text{FOI}(t) + \mu} \quad (\text{S87})$$

$$\Delta I(t) = [1 - \exp(-(\gamma + \mu)\Delta t)] I(t - \Delta t) \quad (\text{S88})$$

$$N_{IR}(t) = \frac{\gamma \Delta I(t)}{\gamma + \mu} \quad (\text{S89})$$

$$\Delta R(t) = [1 - \exp(-(\nu + \mu)\Delta t)] R(t - \Delta t) \quad (\text{S90})$$

$$N_{RS}(t) = \frac{\nu \Delta R(t)}{\nu + \mu} \quad (\text{S91})$$

$$S(t) = S(t - \Delta t) + \mu S - \Delta S(t) + N_{RS}(t) \quad (\text{S92})$$

$$I(t) = I(t - \Delta t) - \Delta I(t) + N_{SI}(t) \quad (\text{S93})$$

$$R(t) = R(t - \Delta t) - \Delta R(t) + N_{IR}(t) \quad (\text{S94})$$

678 where we include an extra term ω to account for external infections. Although actual
679 simulations did not include any external infections, we found that including this term
680 generally helped with model convergence in previous analyses [4]. The transmission
681 rate was divided into a seasonal term $\beta_{\text{seas}}(t)$ (repeated every year) and intervention
682 term $\alpha(t)$, which were estimated jointly:

$$\beta(t) = \beta_{\text{seas}}(t)\alpha(t), \quad (\text{S95})$$

683 where $\alpha < 1$ corresponds to reduction in transmission due to intervention effects. To
684 constrain the smoothness of $\beta_{\text{seas}}(t)$, we imposed cyclic, random-walk priors:

$$\beta_{\text{seas}}(t) \sim \text{Normal}(\beta_{\text{seas}}(t - 1), \sigma) \quad t = 2 \dots 52 \quad (\text{S96})$$

$$\beta_{\text{seas}}(1) \sim \text{Normal}(\beta_{\text{seas}}(52), \sigma) \quad (\text{S97})$$

685 [SWP: I noticed that I forgot to put a prior on σ so need to re-do this but won't
 686 change the results.] We fixed $\alpha(t) = 1$ for all $t < 2020$ and estimate α assuming a
 687 normal prior:

$$\alpha \sim \text{Normal}(1, 0.25). \quad (\text{S98})$$

688 We assumed weakly informative priors on ω and ν :

$$\omega \sim \text{Normal}(0, 200) \quad (\text{S99})$$

$$\nu \sim \text{Normal}(104, 26) \quad (\text{S100})$$

689 We assumed that the true birth/death rates, population sizes, and recovery rates are
 690 known. We note, however, that assuming $\gamma = 1/\text{week}$ actually corresponds to a mean
 691 simulated infectious period of 1.6 weeks, which is much longer than the true value;
 692 this approximation allows us to test whether we can still robustly estimate the in-
 693 trinsic resilience given parameter mis-specification. Initial conditions were estimated
 694 with following priors:

$$S(0) = Ns(0) \quad (\text{S101})$$

$$I(0) = Ni(0) \quad (\text{S102})$$

$$s(0) \sim \text{Uniform}(0, 1) \quad (\text{S103})$$

$$i(0) \sim \text{Half-Normal}(0, 0.001) \quad (\text{S104})$$

695 Finally, the observation model was specified as follows:

$$\text{Cases}(t) \sim \text{Negative-Binomial}(\rho N_{SI}(t), \phi) \quad (\text{S105})$$

$$\rho \sim \text{Half-Normal}(0, 0.02) \quad (\text{S106})$$

$$\phi \sim \text{Half-Normal}(0, 10) \quad (\text{S107})$$

696 where ρ represents the reporting probability and ϕ represents the negative binomial
 697 overdispersion parameter.

698 The model was fitted to four separate time series: (1) incidence time series from
 699 the SIRS model, (2) incidence time series for strain 1 from the two-strain model,
 700 (3) incidence time series for strain 2 from the two-strain model, and (4) combined
 701 incidence time series for strains 1 and 2 from the two-strain model. The model was
 702 fitted using rstan [34, 35]. The resulting posterior distribution was used to calculate
 703 the intrinsic resilience of the seasonally unforced system with the same parameters;
 704 eigenvalues of the discrete-time SIR model were computed by numerically finding
 705 the equilibrium and calculating the Jacobian matrix.

706 **Validations for window-selection criteria**

707 We used stochastic SIRS simulations to identify optimal parameters for the window-
 708 selection criteria that we used for the linear regression for estimating empirical re-
 709 silience. For each simulation, we began by generating a random perturbation $\alpha(t)$

710 from a random set of parameters. First, we drew the duration of perturbation τ_{npi}
 711 from a uniform distribution between 1 and 2 years. Then, we drew independent
 712 normal variables z_i of length $\lfloor 364\tau_{\text{npi}} \rfloor$ with a standard deviation of 0.02 and took a
 713 reverse cumulative sum to obtain a realistic shape for the perturbation:

$$x_n = 1 + \sum_{i=n}^{\lfloor 364\tau_{\text{npi}} \rfloor} z_i, \quad n = 1, \dots, \lfloor 364\tau_{\text{npi}} \rfloor. \quad (\text{S108})$$

714 We repeated this random generation process until less than 10% of x_n exceeds 1—
 715 this was done to prevent the perturbation $\alpha(t)$ stays below 1 (and therefore reduce
 716 transmission) for the most part. Then, we set any values that are above 1 or below 0
 717 as 1 and 0, respectively. Then, we randomly drew the minimum transmission during
 718 perturbation α_{\min} from a uniform distribution between 0.5 and 0.7 and scale x_n to
 719 have a minimum of α_{\min} :

$$x_{\text{scale},n} = \alpha_{\min} + (1 - \alpha_{\min}) \times \frac{x_n - \min x_n}{1 - \min x_n}. \quad (\text{S109})$$

720 This allowed us to simulate a realistically shaped perturbation:

$$\alpha(t) = \begin{cases} 1 & t < 2020 \\ x_{\text{scale},364(t-2020)} & 2020 \leq t < 2020 + \tau_{\text{npi}} \\ 1 & \tau_{\text{npi}} \leq t \end{cases}. \quad (\text{S110})$$

721 Given this perturbation function, we draw \mathcal{R}_0 from a uniform distribution between
 722 1.5 and 4 and the mean duration of immunity $1/\delta$ from a uniform distribution be-
 723 tween 1 and 4. Then, we simulate the stochastic SIRS model from $S(0) = 10^8/\mathcal{R}_0$
 724 and $I(0) = 100$ from 1990 to 2025 and truncate the time series to 2014–2025; if the
 725 epidemic becomes extinct before the end of simulation, we discard that simulation
 726 and start over from the perturbation generation step.

727 For each epidemic simulation, we computed the empirical resilience by varying
 728 the threshold R for the nearest neighbor approach from 4 to 14 with increments of
 729 2, the number of divisions K for the window selection between 8 and 25, and the
 730 truncation threshold a for the window selection between 1 to 3; this was done for all
 731 possible combinations of R , K , and a . We also compared this with the naive approach
 732 that uses the entire distance-from-attractor time series, starting from the maximum
 733 distance to the end of the time series. We repeated this procedure 500 times and
 734 quantified the correlation between empirical and intrinsic resilience estimates across
 735 two approaches.

Supplementary Figures

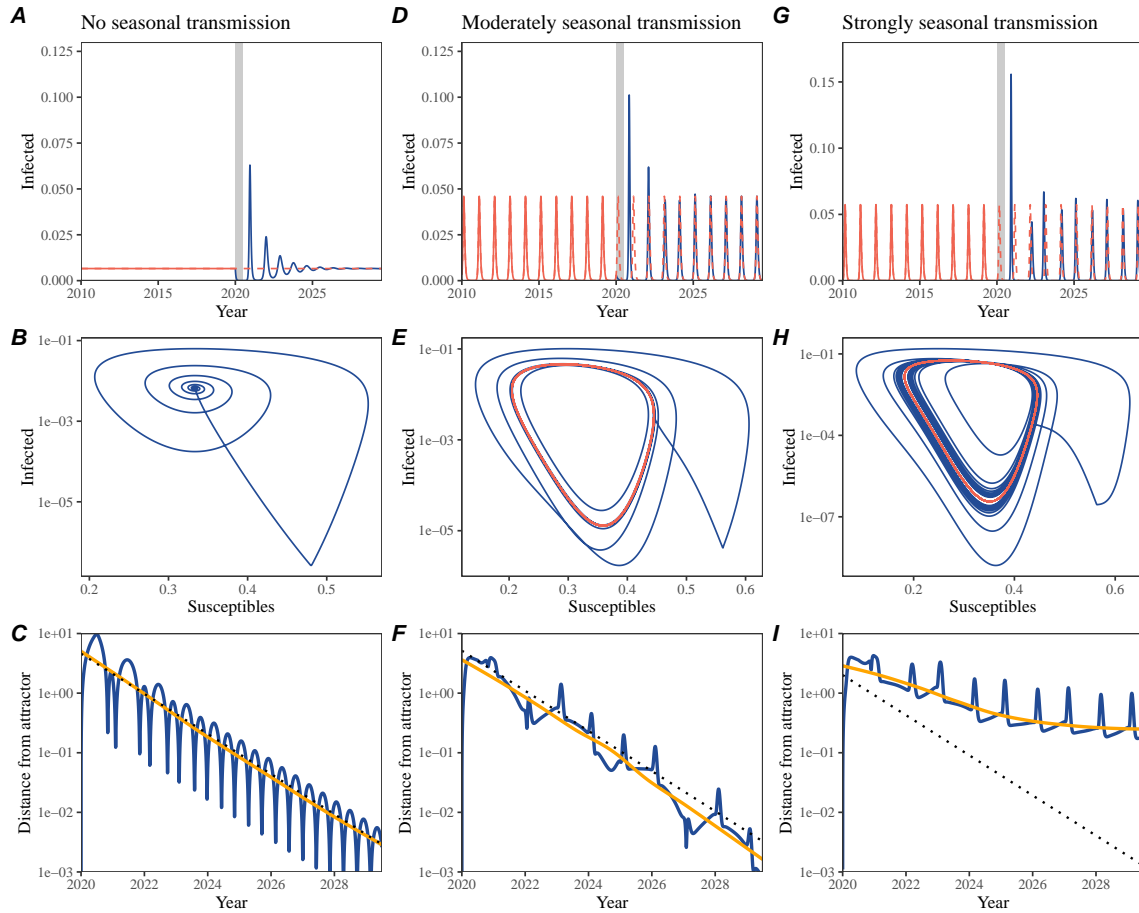


Figure S1: Impact of seasonal transmission on pathogen resilience. (A, D, G) Simulated epidemic trajectories using the SIRS model without seasonal forcing (A), with seasonal forcing of amplitude of 0.2 (D), and with seasonal forcing of amplitude of 0.4 (G). Red and blue solid lines represent epidemic dynamics before and after interventions are introduced, respectively. Red dashed lines represent counterfactual epidemic dynamics in the absence of interventions. Gray regions indicate the duration of interventions. (B, E, H) Phase plane representation of the time series in panels A, D, and G alongside the corresponding susceptible host dynamics. Red and blue solid lines represent epidemic trajectories on an SI phase plane before and after interventions are introduced, respectively. (C, F, I) Changes in logged distance from the attractor over time. Blue lines represent the logged distance from the attractor. Orange lines represent the locally estimated scatterplot smoothing (LOESS) fits to the logged distance from the attractor. Dotted lines show the intrinsic resilience of the seasonally unforced system.

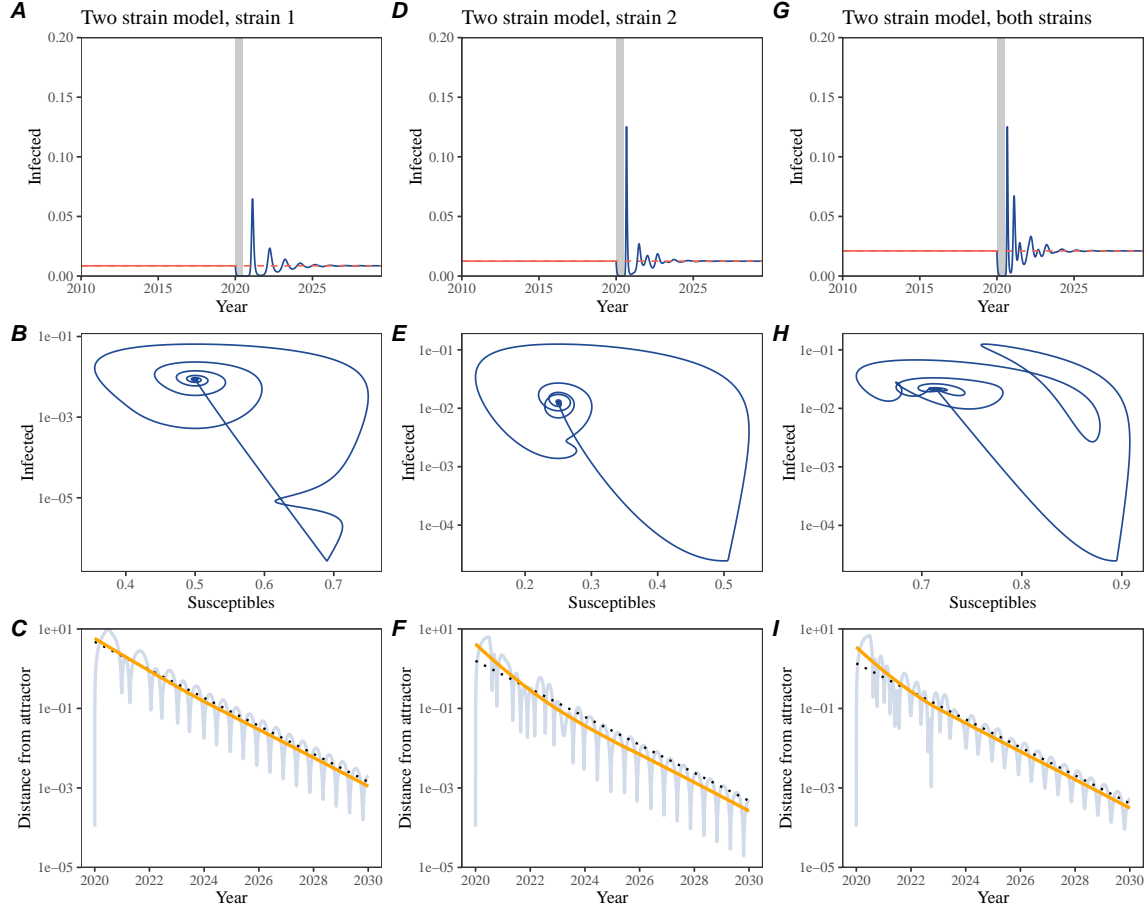


Figure S2: A simple method to measure pathogen resilience following pandemic perturbations for a two-strain system without seasonal forcing. (A, D, G) Simulated epidemic trajectories using a multi-strain system without seasonal forcing. Red and blue solid lines represent epidemic dynamics before and after interventions are introduced, respectively. Red dashed lines represent counterfactual epidemic dynamics in the absence of interventions. Gray regions indicate the duration of interventions. (B, E, H) Phase plane representation of the time series in panels A, D, and G alongside the corresponding susceptible host dynamics. Blue solid lines represent epidemic trajectories on an SI phase plane before and after interventions are introduced, respectively. (C, F, I) Changes in logged distance from the attractor over time. Blue lines represent the logged distance from the attractor. Orange lines represent the locally estimated scatterplot smoothing (LOESS) fits to the logged distance from the attractor. Dotted lines show the intrinsic resilience of the seasonally unforced system.

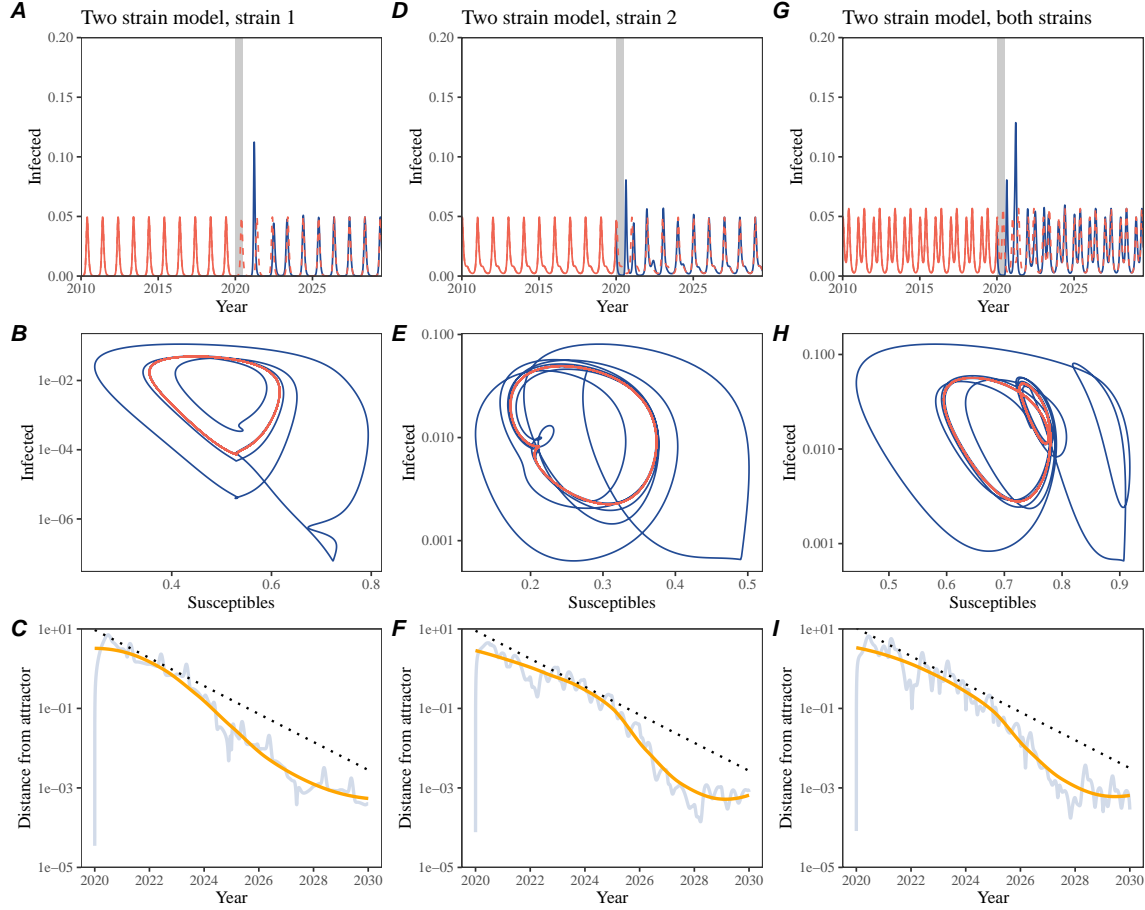


Figure S3: A simple method to measure pathogen resilience following pandemic perturbations for a two-strain system with seasonal forcing. (A, D, G) Simulated epidemic trajectories using a two-strain system with seasonal forcing (amplitude of 0.2). In this model, two strains compete through cross immunity. Red and blue solid lines represent epidemic dynamics before and after interventions are introduced, respectively. Red dashed lines represent counterfactual epidemic dynamics in the absence of interventions. Gray regions indicate the duration of interventions. (B, E, H) Phase plane representation of the time series in panels A, D, and G alongside the corresponding susceptible host dynamics. Red and blue solid lines represent epidemic trajectories on an SI phase plane before and after interventions are introduced, respectively. (C, F, I) Changes in logged distance from the attractor over time. Blue lines represent the logged distance from the attractor. Orange lines represent the locally estimated scatterplot smoothing (LOESS) fits to the logged distance from the attractor. Dotted lines show the intrinsic resilience of the seasonally unforced system.

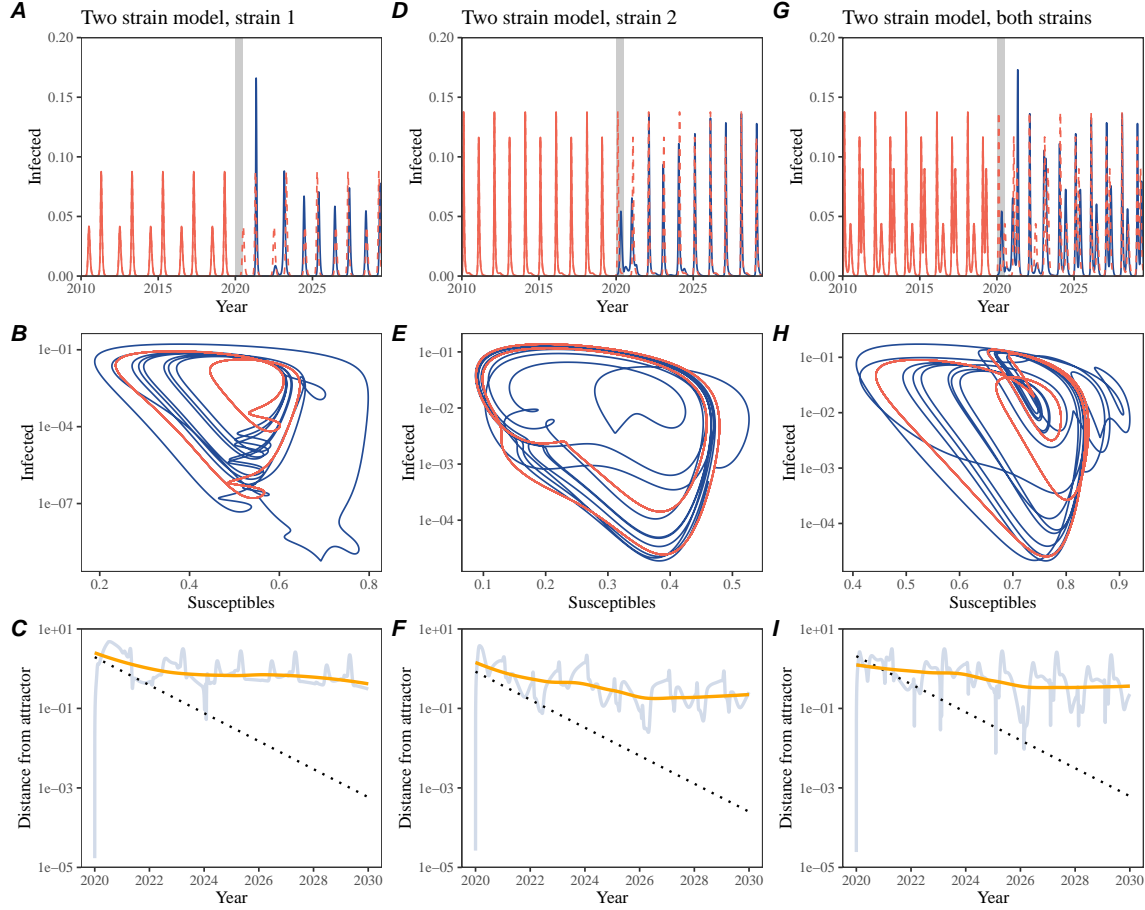


Figure S4: A simple method to measure pathogen resilience following pandemic perturbations for a multi-strain system with strong seasonal forcing. (A, D, G) Simulated epidemic trajectories using a multi-strain system with seasonal forcing (amplitude of 0.4). In this model, two strains compete through cross immunity. Red and blue solid lines represent epidemic dynamics before and after interventions are introduced, respectively. Red dashed lines represent counterfactual epidemic dynamics in the absence of interventions. Gray regions indicate the duration of interventions. (B, E, H) Phase plane representation of the time series in panels A, D, and G alongside the corresponding susceptible host dynamics. Red and blue solid lines represent epidemic trajectories on an SI phase plane before and after interventions are introduced, respectively. (C, F, I) Changes in logged distance from the attractor over time. Blue lines represent the logged distance from the attractor. Orange lines represent the locally estimated scatterplot smoothing (LOESS) fits to the logged distance from the attractor. Dotted lines show the intrinsic resilience of the seasonally unforced system.

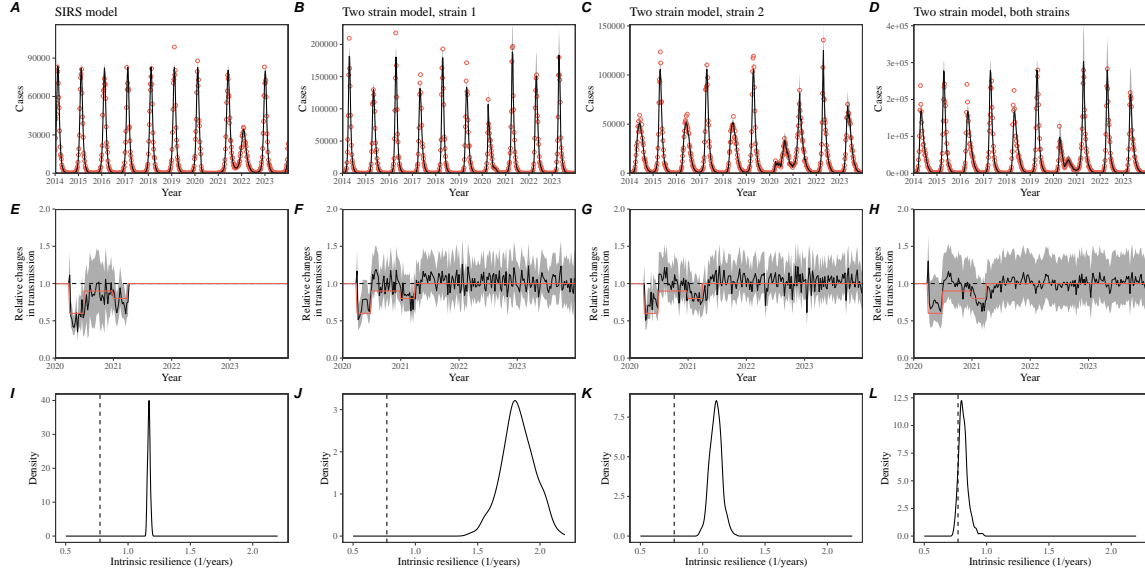


Figure S5: Mechanistic model fits to simulated data and inferred intrinsic resilience. We simulated discrete time, stochastic epidemic trajectories using seasonally forced SIRS model (A,E,I) and seasonally forced two-strain model (B–D, F–H, and J–L) and tested whether we can estimate the intrinsic resilience of the seasonally unforced versions of the model by fitting a mechanistic model (Supplementary Text). We fitted the same discrete time, deterministic SIRS model across all four scenarios. (A–D) Simulated case time series from corresponding models shown in the title (red) and SIRS model fits (black). (E–H) Assumed changes in transmission due to pandemic perturbations (red) and estimated time-varying relative transmission rates for the perturbation impact from the SIRS model fits (black). Solid lines and shaded regions represent fitted posterior median and 95% credible intervals. (I–L) True intrinsic resilience of the seasonally unforced system (vertical lines) and the posterior distribution of the inferred intrinsic resilience from the SIRS model (density plots).

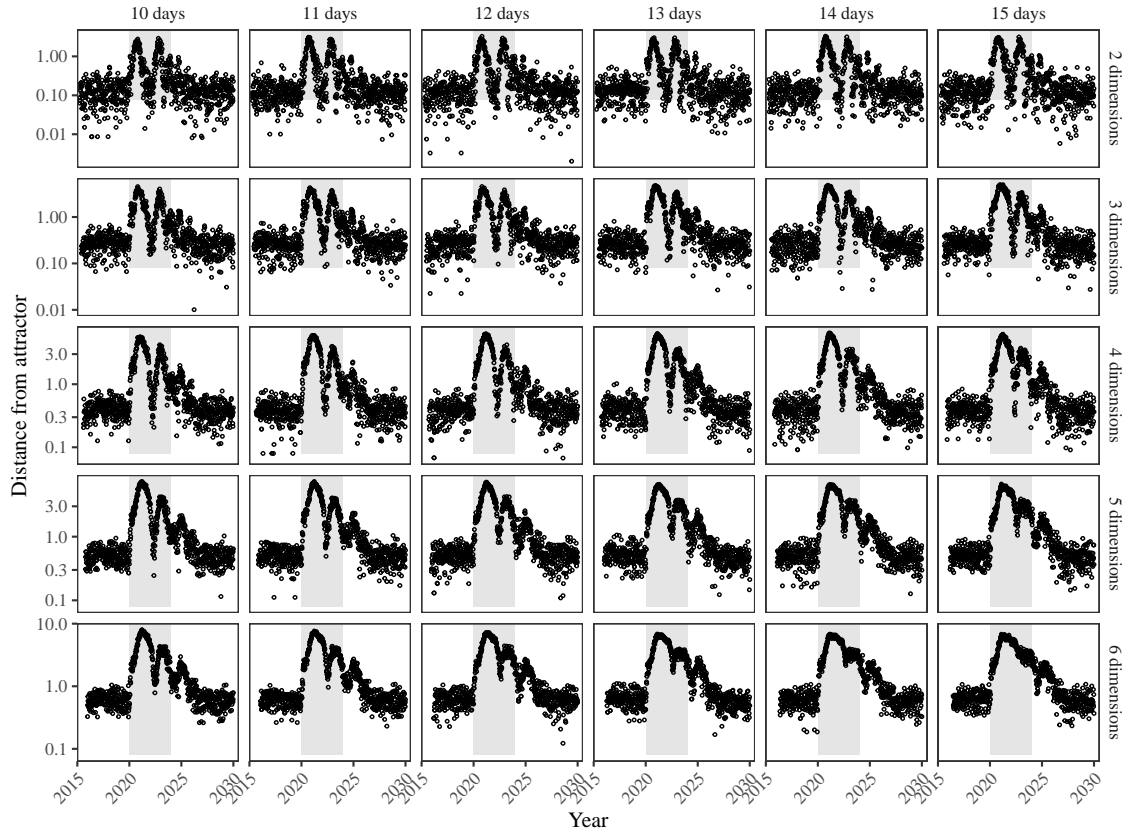


Figure S6: Sensitivity of the distance from the attractor to choices about embedding lags and dimensions. Sensitivity analysis for the distance-from-attractor time series shown in Figure 3E in the main text by varying the embedding lag between 10–15 days and embedding dimensions between 2–6 dimensions. [SWP: You said: “Did you do sensitivity analyses with other systems or just this one? I think we’ll probably need to do it with several systems”. I think it’s OK to just do this because we’re just trying to show qualitatively that longer lags and higher dimensions smooth things out. We also explore resilience of other models in other figures.]

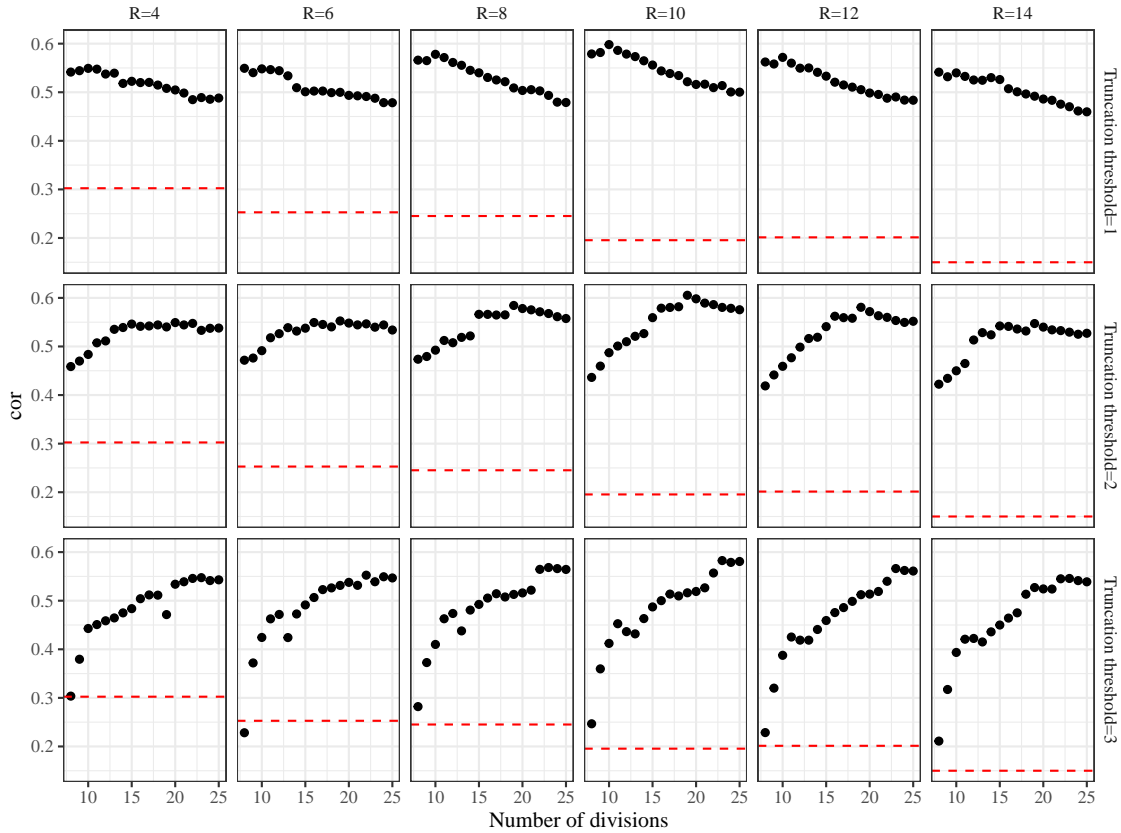


Figure S7: Impact of fitting window selection on the estimation of empirical resilience. We simulated 500 epidemics of a stochastic SIRS model with randomly drawn parameters and randomly generated pandemic perturbations (Supplementary Text). For each simulation, we varied the false nearest neighbor threshold R for reconstructing the empirical attractor as well as the parameters for regression window selection (i.e., the truncation threshold a and the the number of divisions K). Each point represents the resulting correlation coefficient between empirical and intrinsic resilience estimates for a given scenario. Dashed lines represent the correlation coefficient between empirical and intrinsic resilience estimates for the naive approach that fits a linear regression on a log scale, starting from the maximum distance until the end of the time series.

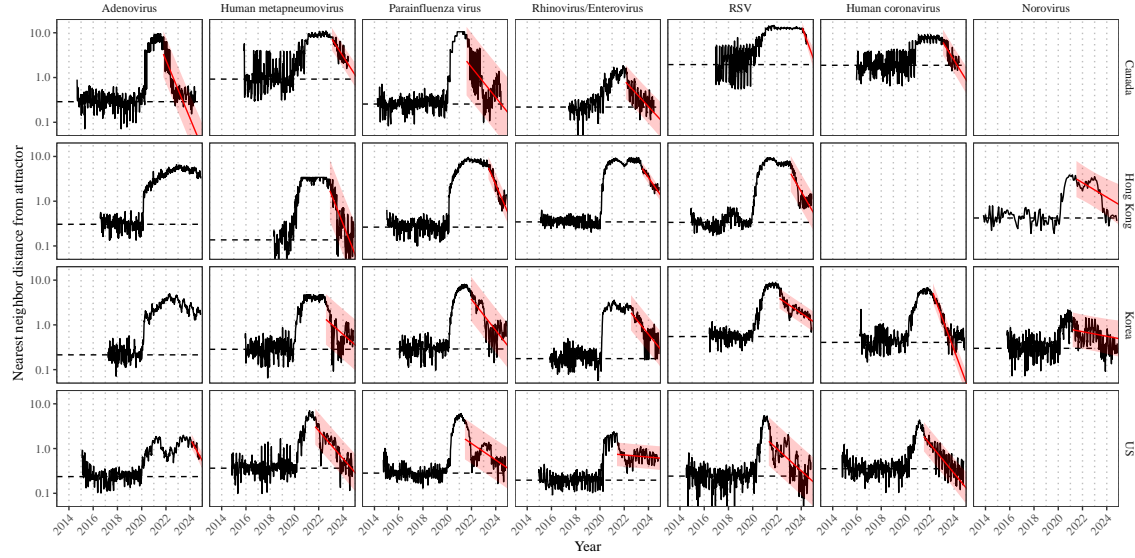


Figure S8: Estimated time series of distance from the attractor for each pathogen and corresponding linear regression fits using automated window selection criterion across Canada, Hong Kong, Korea, and the US. Black lines represent the estimated distance from the attractor. Red lines and shaded regions represent the linear regression fits and corresponding 95% confidence intervals. Dashed lines represent the average of the pre-pandemic nearest neighbor distances.

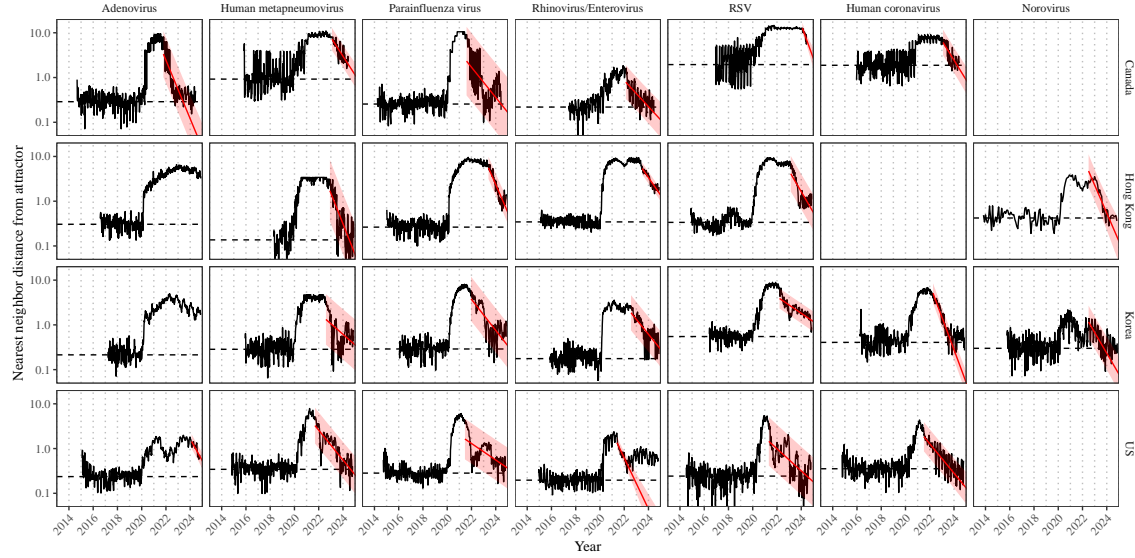


Figure S9: Estimated time series of distance from the attractor for each pathogen and corresponding linear regression fits across Canada, Hong Kong, Korea, and the US, including ad-hoc regression window selection. We used ad-hoc regression windows for norovirus in Hong Kong and Korea and Rhinovirus/Enterovirus in the US. Black lines represent the estimated distance from the attractor. Red lines and shaded regions represent the linear regression fits and corresponding 95% confidence intervals. Dashed lines represent the average of the pre-pandemic nearest neighbor distances.

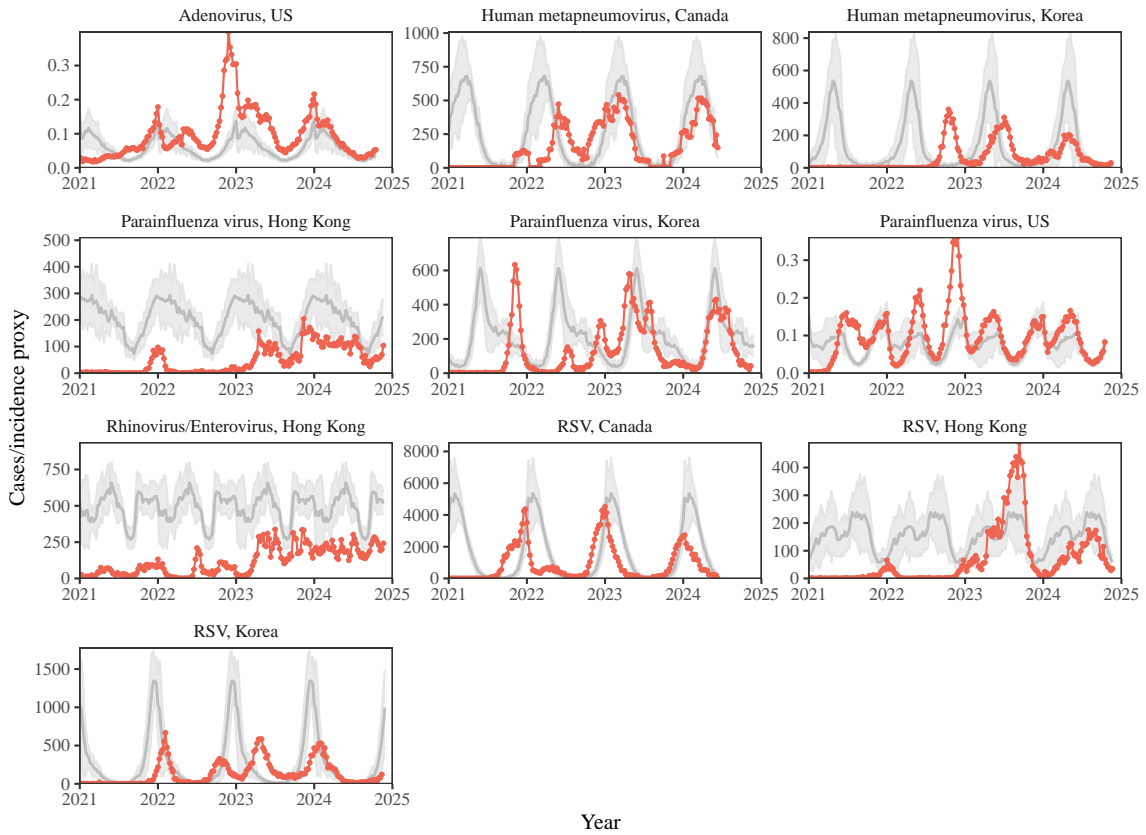


Figure S10: Observed dynamics for pathogen that are predicted to return after the end of 2024. Red points and lines represent data before 2020. Gray lines and shaded regions represent the mean seasonal patterns and corresponding 95% confidence intervals around the mean, previously shown in Figure 1.

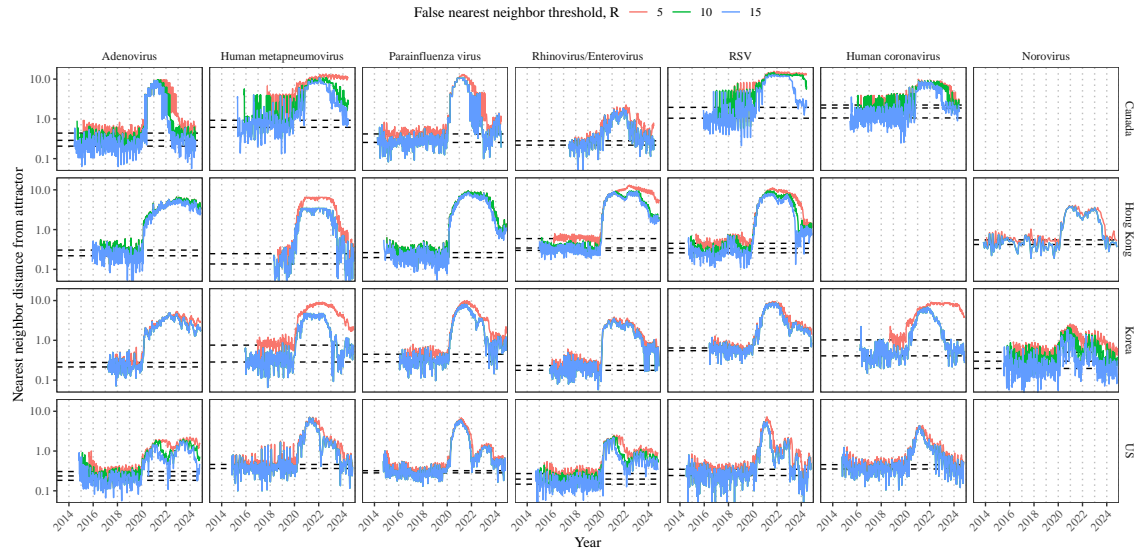


Figure S11: Estimated time series of distance from the attractor for each pathogen across different choices about false nearest neighbor threshold values. Using higher threshold values for the false nearest neighbor approach gives lower embedding dimensions. Colored lines represent the estimated distance from the attractor for different threshold values.

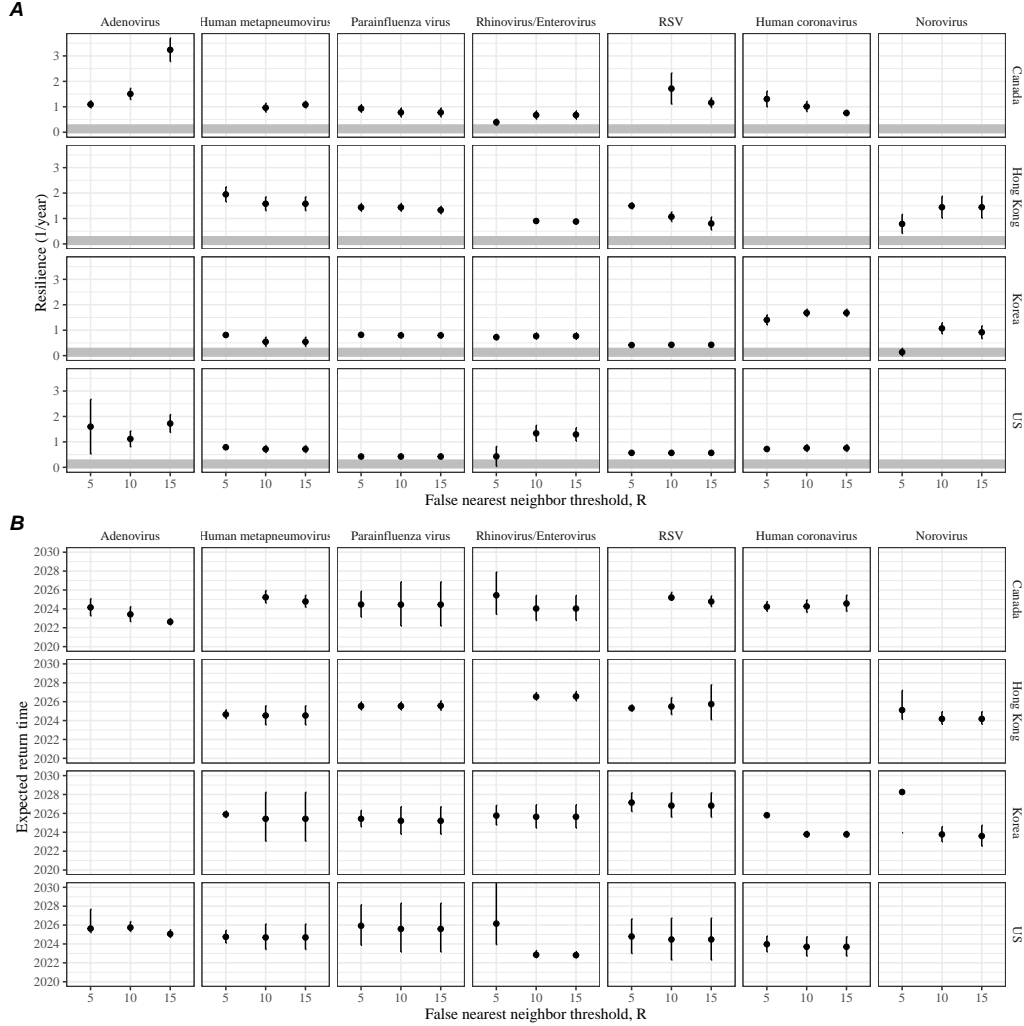


Figure S12: **Summary of resilience estimates and predictions for return time across different choices about false nearest neighbor threshold values.** The automated window selection method was used for all scenarios to estimate pathogen resilience, except for norovirus in Hong Kong and Korea and Rhinovirus/Enterovirus in the US. We used the same ad-hoc regression windows for norovirus in Hong Kong and Korea and Rhinovirus/Enterovirus in the US as we did in the main analysis. (A) Estimated pathogen resilience. The gray horizontal line represents the intrinsic resilience of pre-vaccination measles dynamics. (B) Predicted timing of when each pathogen will return to their pre-pandemic cycles. The dashed line in panel B indicates the end of 2024 (current observation time). Error bars represent 95% confidence intervals.

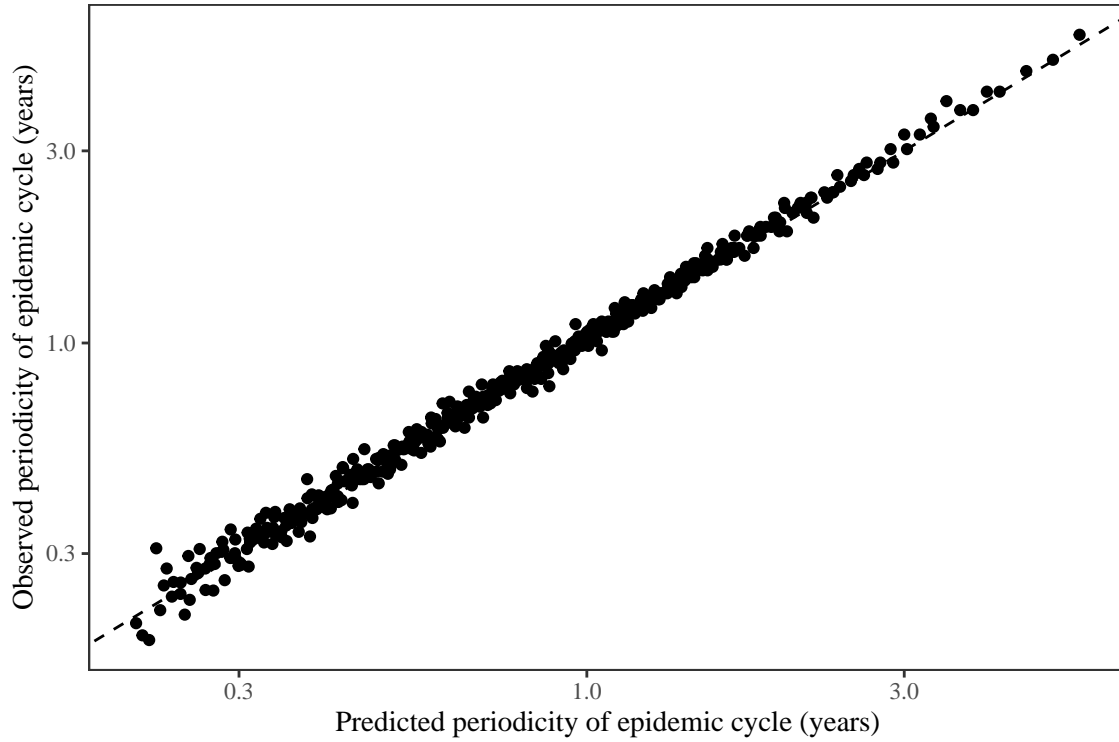


Figure S13: **Comparison between the observed and predicted periodicity of the epidemic cycle of the seasonally unforced SIRS model.** The observed periodicity of the epidemic corresponds to the periodicity at which maximum spectral density occurs. The predicted periodicity of the epidemic corresponds to $2\pi/\text{Im}(\lambda)$, where $\text{Im}(\lambda)$ is the imaginary part of the eigenvalue.

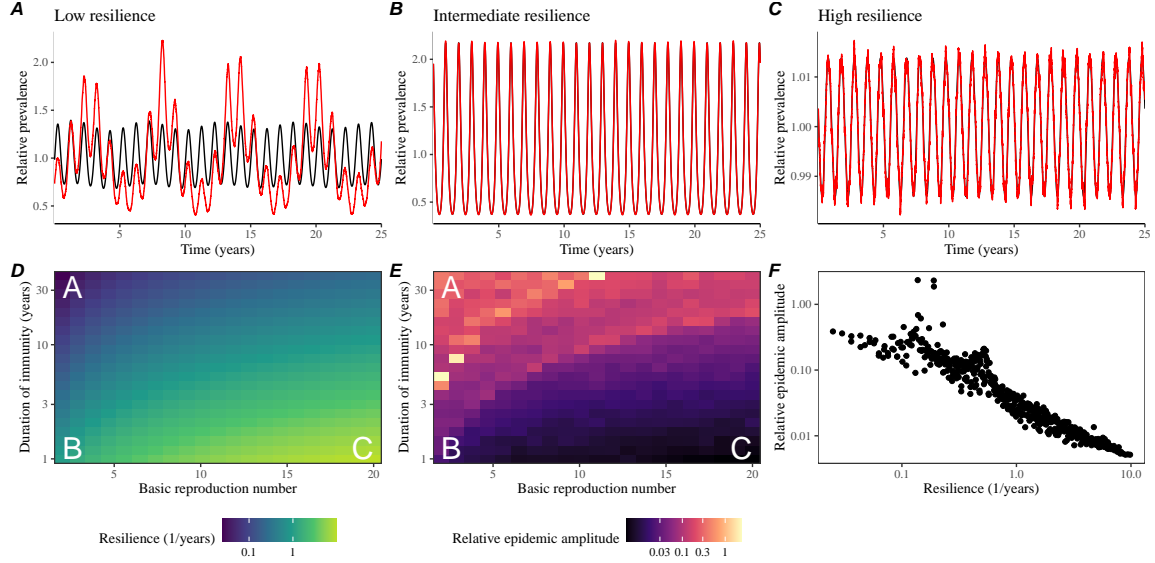


Figure S14: Linking resilience of a host-pathogen system to its sensitivity to stochastic perturbations for the seasonally forced SIRS model. (A–C) Epidemic trajectories of a stochastic SIRS model across three different resilience values: low, intermediate, and high. The relative prevalence was calculated by dividing infection prevalence by its mean value. (D) The heat map represents the intrinsic resilience of the seasonally unforced system as a function of the basic reproduction number \mathcal{R}_0 and the duration of immunity. (E) The heat map represents the relative epidemic amplitude as a function of the basic reproduction number \mathcal{R}_0 and the duration of immunity. To calculate the relative epidemic amplitude, we first take the relative difference in infection prevalence between stochastic and deterministic trajectories: $\epsilon = (I_{\text{stoch}} - I_{\text{det}})/I_{\text{det}}$. Then, we calculate the difference between maximum and minimum of the relative difference and divide by half: $(\max \epsilon - \min \epsilon)/2$. (F) The relationship between pathogen resilience and relative epidemic amplitude.

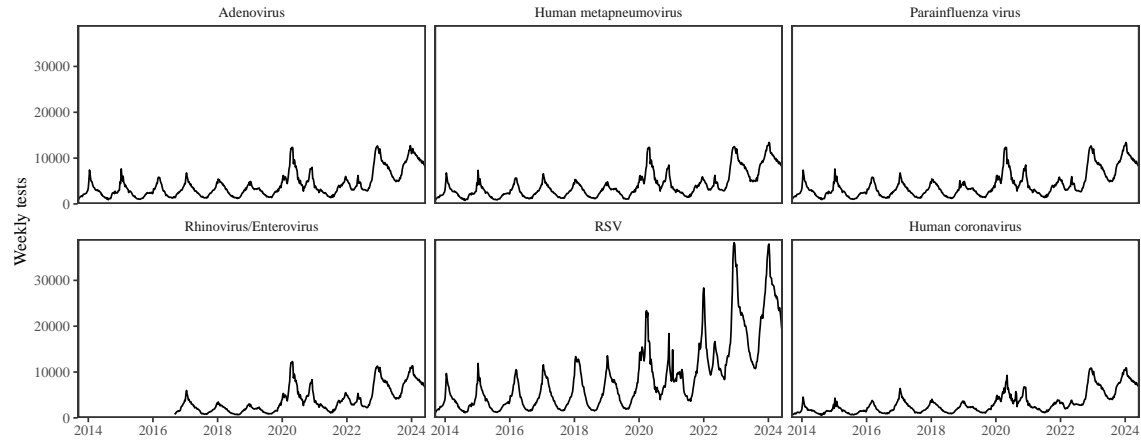


Figure S15: Testing patterns for respiratory pathogens in Canada.

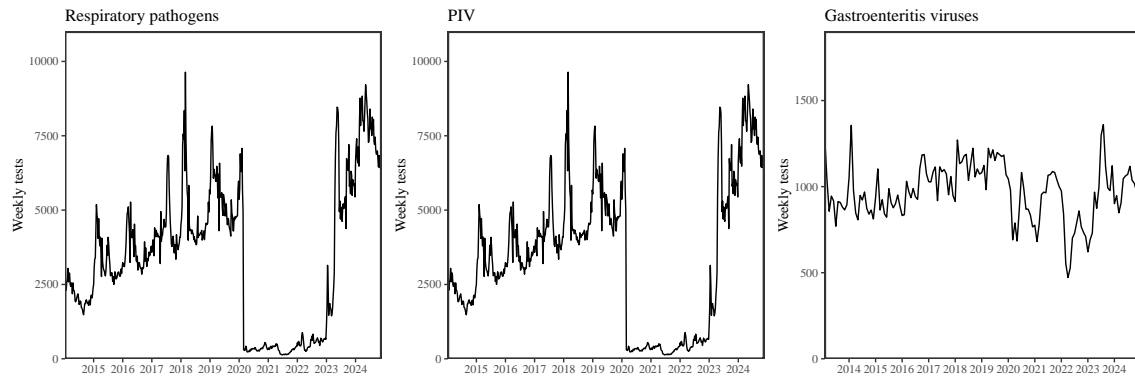


Figure S16: Testing patterns for respiratory pathogens, PIV, and gastroenteritis viruses in Hong Kong.

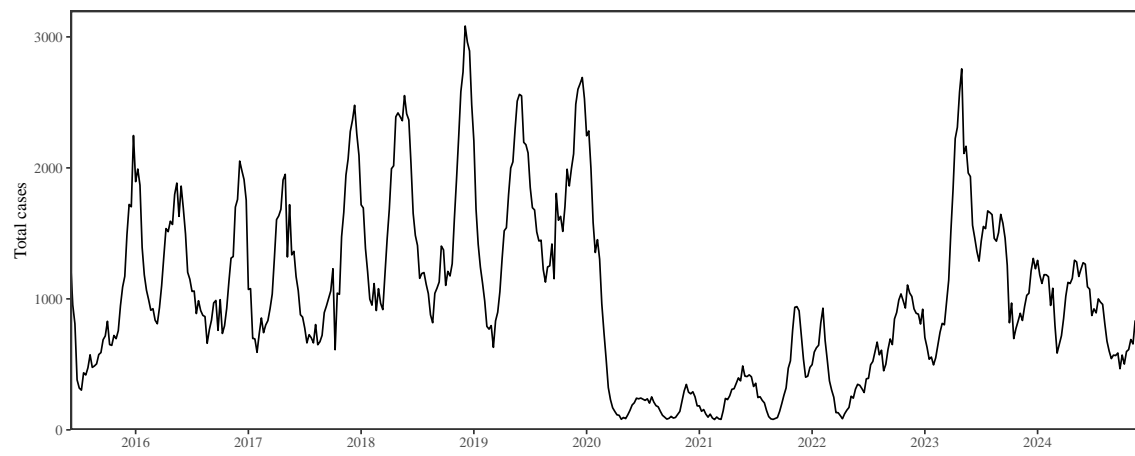


Figure S17: Total number of reported respiratory infection cases in Korea.

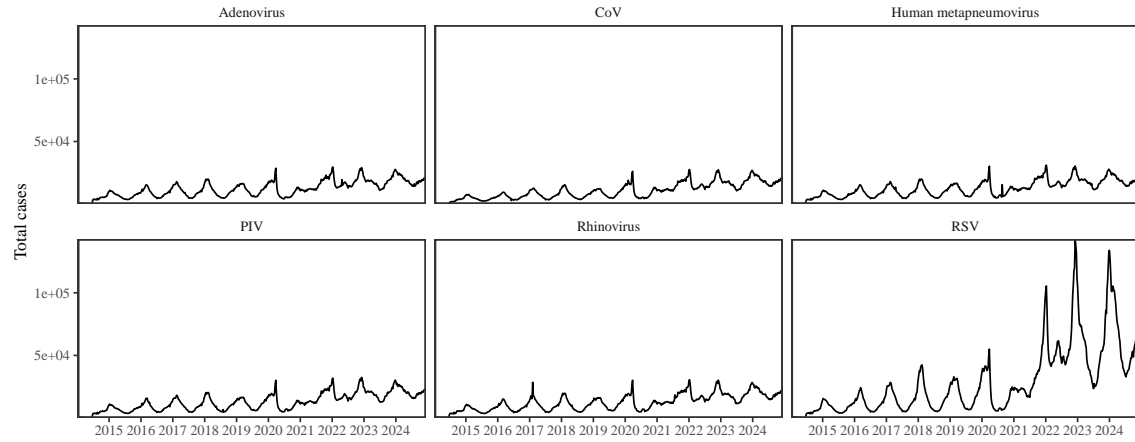


Figure S18: Testing patterns for respiratory pathogens in the US reported through the NREVSS.

737 **References**

- 738 [1] Rachel E Baker, Sang Woo Park, Wenchang Yang, Gabriel A Vecchi, C Jessica E
739 Metcalf, and Bryan T Grenfell. The impact of COVID-19 nonpharmaceutical
740 interventions on the future dynamics of endemic infections. *Proceedings of the*
741 *National Academy of Sciences*, 117(48):30547–30553, 2020.
- 742 [2] Gabriela B Gomez, Cedric Mahé, and Sandra S Chaves. Uncertain effects of the
743 pandemic on respiratory viruses. *Science*, 372(6546):1043–1044, 2021.
- 744 [3] Mihaly Koltai, Fabienne Krauer, David Hodgson, Edwin van Leeuwen, Marina
745 Treskova-Schwarzbach, Mark Jit, and Stefan Flasche. Determinants of RSV
746 epidemiology following suppression through pandemic contact restrictions. *Epi-*
747 *demics*, 40:100614, 2022.
- 748 [4] Sang Woo Park, Brooklyn Noble, Emily Howerton, Bjarke F Nielsen, Sarah
749 Lentz, Lilliam Ambroggio, Samuel Dominguez, Kevin Messacar, and Bryan T
750 Grenfell. Predicting the impact of non-pharmaceutical interventions against
751 COVID-19 on *Mycoplasma pneumoniae* in the United States. *Epidemics*,
752 49:100808, 2024.
- 753 [5] Amanda C Perofsky, Chelsea L Hansen, Roy Burstein, Shanda Boyle, Robin
754 Prentice, Cooper Marshall, David Reinhart, Ben Capodanno, Melissa Truong,
755 Kristen Schwabe-Fry, et al. Impacts of human mobility on the citywide trans-
756 mission dynamics of 18 respiratory viruses in pre-and post-COVID-19 pandemic
757 years. *Nature communications*, 15(1):4164, 2024.
- 758 [6] Eric J Chow, Timothy M Uyeki, and Helen Y Chu. The effects of the COVID-19
759 pandemic on community respiratory virus activity. *Nature Reviews Microbiol-*
760 *ogy*, 21(3):195–210, 2023.
- 761 [7] Stephen M Kissler, Christine Tedijanto, Edward Goldstein, Yonatan H Grad,
762 and Marc Lipsitch. Projecting the transmission dynamics of SARS-CoV-2
763 through the postpandemic period. *Science*, 368(6493):860–868, 2020.
- 764 [8] Rachel E Baker, Chadi M Saad-Roy, Sang Woo Park, Jeremy Farrar, C Jessica E
765 Metcalf, and Bryan T Grenfell. Long-term benefits of nonpharmaceutical inter-
766 ventions for endemic infections are shaped by respiratory pathogen dynamics.
767 *Proceedings of the National Academy of Sciences*, 119(49):e2208895119, 2022.
- 768 [9] John-Sebastian Eden, Chisha Sikazwe, Ruopeng Xie, Yi-Mo Deng, Sheena G
769 Sullivan, Alice Michie, Avram Levy, Elena Cutmore, Christopher C Blyth,
770 Philip N Britton, et al. Off-season RSV epidemics in Australia after easing
771 of COVID-19 restrictions. *Nature communications*, 13(1):2884, 2022.
- 772 [10] Stuart L Pimm. The structure of food webs. *Theoretical population biology*,
773 16(2):144–158, 1979.

- 774 [11] Michael G Neubert and Hal Caswell. Alternatives to resilience for measuring
775 the responses of ecological systems to perturbations. *Ecology*, 78(3):653–665,
776 1997.
- 777 [12] Lance H Gunderson. Ecological resilience—in theory and application. *Annual
778 review of ecology and systematics*, 31(1):425–439, 2000.
- 779 [13] Vasilis Dakos and Sonia Kéfi. Ecological resilience: what to measure and how.
780 *Environmental Research Letters*, 17(4):043003, 2022.
- 781 [14] Floris Takens. Detecting strange attractors in turbulence. In *Dynamical Sys-
782 tems and Turbulence, Warwick 1980: proceedings of a symposium held at the
783 University of Warwick 1979/80*, pages 366–381. Springer, 2006.
- 784 [15] Jonathan Dushoff, Joshua B Plotkin, Simon A Levin, and David JD Earn. Dynamical resonance can account for seasonality of influenza epidemics. *Pro-
785 ceedings of the National Academy of Sciences*, 101(48):16915–16916, 2004.
- 787 [16] Alan Hastings, Karen C Abbott, Kim Cuddington, Tessa Francis, Gabriel Gell-
788 ner, Ying-Cheng Lai, Andrew Morozov, Sergei Petrovskii, Katherine Scran-
789 ton, and Mary Lou Zeeman. Transient phenomena in ecology. *Science*,
790 361(6406):eaat6412, 2018.
- 791 [17] Matthew B Kennel, Reggie Brown, and Henry DI Abarbanel. Determining
792 embedding dimension for phase-space reconstruction using a geometrical con-
793 struction. *Physical review A*, 45(6):3403, 1992.
- 794 [18] Eugene Tan, Shannon Algar, Débora Corrêa, Michael Small, Thomas Stemler,
795 and David Walker. Selecting embedding delays: An overview of embedding
796 techniques and a new method using persistent homology. *Chaos: An Interdis-
797 ciplinary Journal of Nonlinear Science*, 33(3), 2023.
- 798 [19] Jennifer M Radin, Anthony W Hawksworth, Peter E Kammerer, Melinda Bal-
799 ansay, Rema Raman, Suzanne P Lindsay, and Gary T Brice. Epidemiology
800 of pathogen-specific respiratory infections among three US populations. *PLoS
801 One*, 9(12):e114871, 2014.
- 802 [20] Guojian Lv, Limei Shi, Yi Liu, Xuecheng Sun, and Kai Mu. Epidemiological
803 characteristics of common respiratory pathogens in children. *Scientific Reports*,
804 14(1):16299, 2024.
- 805 [21] Saverio Caini, Adam Meijer, Marta C Nunes, Laetitia Henaff, Malaika Zounon,
806 Bronke Boudewijns, Marco Del Riccio, and John Paget. Probable extinction of
807 influenza b/yamagata and its public health implications: a systematic literature
808 review and assessment of global surveillance databases. *The Lancet Microbe*,
809 2024.

- 810 [22] Zhiyuan Chen, Joseph L-H Tsui, Bernardo Gutierrez, Simon Busch Moreno,
811 Louis du Plessis, Xiaowei Deng, Jun Cai, Sumali Bajaj, Marc A Suchard,
812 Oliver G Pybus, et al. COVID-19 pandemic interventions reshaped the global
813 dispersal of seasonal influenza viruses. *Science*, 386(6722):eadq3003, 2024.
- 814 [23] Bryan T Grenfell, Ottar N Bjørnstad, and Bärbel F Finkenstädt. Dynamics of
815 measles epidemics: scaling noise, determinism, and predictability with the TSIR
816 model. *Ecological monographs*, 72(2):185–202, 2002.
- 817 [24] Samit Bhattacharyya, Per H Gesteland, Kent Korgenski, Ottar N Bjørnstad,
818 and Frederick R Adler. Cross-immunity between strains explains the dynamical
819 pattern of paramyxoviruses. *Proceedings of the National Academy of Sciences*,
820 112(43):13396–13400, 2015.
- 821 [25] Virginia E Pitzer, Cécile Viboud, Wladimir J Alonso, Tanya Wilcox, C Jessica
822 Metcalf, Claudia A Steiner, Amber K Haynes, and Bryan T Grenfell. Environmental
823 drivers of the spatiotemporal dynamics of respiratory syncytial virus in
824 the United States. *PLoS pathogens*, 11(1):e1004591, 2015.
- 825 [26] Katharine R Dean, Fabienne Krauer, Lars Walløe, Ole Christian Lingjærde, Barbara
826 Bramanti, Nils Chr Stenseth, and Boris V Schmid. Human ectoparasites
827 and the spread of plague in Europe during the Second Pandemic. *Proceedings
828 of the National Academy of Sciences*, 115(6):1304–1309, 2018.
- 829 [27] Margarita Pons-Salort and Nicholas C Grassly. Serotype-specific immunity
830 explains the incidence of diseases caused by human enteroviruses. *Science*,
831 361(6404):800–803, 2018.
- 832 [28] Sarah Cobey and Edward B Baskerville. Limits to causal inference with state-
833 space reconstruction for infectious disease. *PloS one*, 11(12):e0169050, 2016.
- 834 [29] Public Health Agency of Canada. Respiratory virus detections in
835 Canada. 2024. <https://www.canada.ca/en/public-health/services/surveillance/respiratory-virus-detections-canada.html>. Accessed Sep
836 4, 2024.
- 837 [30] Centre for Health Protection. Detection of pathogens from respiratory spec-
imens. 2024. <https://www.chp.gov.hk/en/statistics/data/10/641/642/2274.html>. Accessed Nov 20, 2024.
- 838 [31] Centre for Health Protection. Detection of gastroenteritis viruses from faecal
specimens. 2024. <https://www.chp.gov.hk/en/statistics/data/10/641/717/3957.html>. Accessed Nov 20, 2024.
- 839 [32] Korea Disease Control and Prevention Agency. Acute respiratory infection,
840 Sentinel surveillance infectious diseases. 2024. <https://dportal.kdca.go.kr/pot/is/st/ari.do>. Accessed Nov 20, 2024.

- 847 [33] Edward Goldstein, Sarah Cobey, Saki Takahashi, Joel C Miller, and Marc Lip-
848 sitch. Predicting the epidemic sizes of influenza A/H1N1, A/H3N2, and B: a
849 statistical method. *PLoS medicine*, 8(7):e1001051, 2011.
- 850 [34] Bob Carpenter, Andrew Gelman, Matthew D Hoffman, Daniel Lee, Ben
851 Goodrich, Michael Betancourt, Marcus A Brubaker, Jiqiang Guo, Peter Li,
852 and Allen Riddell. Stan: A probabilistic programming language. *Journal of*
853 *statistical software*, 76, 2017.
- 854 [35] Stan Development Team. RStan: the R interface to Stan, 2024. R package
855 version 2.32.6.